IT'IS FOUNDATION

Foundation for Research on Information Technologies in Society

Prof. Dr. Niels Kuster

Director Foundation IT'IS
Professor of Swiss Federal Institute of Technology – ETHZ
Phone +41 44 245 9690 · kuster@itis.ethz.ch

Final Report

Assessment of EM Exposure of Energy-Saving Bulbs & Possible Mitigation Strategies

Project BAG/08.004316/434.0001/-13 & BFE/15350

Jagadish Nadakuduti, Mark Douglas, Myles Capstick, Sven Kühn, Stefan Benkler, Niels Kuster

Zürich, March 21, 2010

Executive Summary

The objective of this project is the development of scientifically sound instrumentation, methods and procedures for the EM exposure assessment of energy-saving bulbs (ESBs). Previous investigations and our initial incident field measurements have demonstrated that compliance tests cannot be performed using standard free-space equipment, since the reference levels are exceeded in the close vicinity of the light bulbs. The uncertainty of free-space measurements close to the bulbs is also very large, due to the large size of the sensors. The uncertainty is approximately ± 3 dB (± 40%) at 300 mm and will be much larger at very close distances. The recently defined standard IEC 62493 [1] is also inadequate since it is based on incident fields at an arbitrary larger distance from the bulbs (i.e., neglecting the regions of large field strength close to the bulbs) and not providing any correlation to the exposure in people.

In order to obtain a sound testing of compliance with the basic restrictions in the safety guidelines, novel equipment had to be developed for the measurement of the field values induced inside the human body. This equipment has been developed and a first prototype built, characterized and validated. The authors have also established a relationship between the measured induced current densities and the values induced in different human bodies and in various postures.

The field levels in eleven compact fluorescent ESBs, two long fluorescent tube lights, two incandescent bulbs and two LED bulbs have been measured. The results show that the primary coupling of induced current densities in the body is from the electric fields surrounding the bulbs rather than the magnetic field. For the light bulbs studied, the maximum induced current densities (at a distance of 20 mm) were comparable to the ICNIRP limits after adjusting for exposure in human body models (relative values ranged from 9% to 56% as shown in Table 20).

Over the frequency range investigated, the measured induced field levels were considerably higher for ESBs (0.84 mA/m^2 to 8.6 mA/m^2) than for LED bulbs (0.5 mA/m^2) or incandescent bulbs (within the noise level of the equipment), as shown in Table 10. The study does not represent a market overview, because not all lamps available on the market have been investigated. Thus it cannot be concluded from this study that energy saving lamps *per se* meet the ICNIRP Guidelines. Measurements of a sample of ten bulbs of the same manufacturer and model found that the variations are within the measurement uncertainty.

The measurement uncertainty of the current density probe was estimated to be 17%. The uncertainty of the conservative factors used to correlate the measured values to the induced current densities in human models is estimated to be less than 20%.

Mitigation strategies for light bulb exposure have been investigated. As expected, exposure generally increases with higher output power. However, there is considerable variation in the exposure for light bulbs having the same rated output power. The variations between different ESB models were greater than a factor of two, depending on the construction. Therefore, manufacturers can take care of the design to reduce the exposure. At locations very close to the light bulb, exposure drops strongly with distance.

In conclusion, the worst-case exposure of all investigated bulbs at a separation of 20 mm were within the ICNIRP limits, the majority of which with large margins. The maximum induced current density drops by a factor of 5 after moving 200 mm away from the bulb. However, based on the observed large variations between the bulbs, it can not be concluded that energy saving bulbs are intrinsically compliant with the ICNIRP recommendations. The exposures of the incandescent and LED bulbs were below the sensitivity of the equipment. We found that the recently defined standard procedure of IEC 62493 [1] is inadequate for determining the EM exposure of bulbs. The IEC 62493 standard can be improved by adopting the procedures and equipment described in this report.

Contents

1 Introduction

Compact fluorescent energy saving bulbs (ESBs) generate electromagnetic fields at frequencies in the kHz range. As with other electrical appliances, they also generate extremely low frequency (ELF) fields. The human health risks posed by exposure to these bulbs have been assessed by the Research Foundation for Mobile Communication [2], [3], [4], as mandated by the Swiss Federal Office of Energy (SFOE) and the Swiss Federal Office of Public Health, and a study conducted by Dr. Heinrich Eder [5], Landesamt für Umwelt, Germany. The results of these studies were inconsistent, and the review [6] suggested that the applied procedures and equipment were inadequate, i.e., no definite conclusions could be drawn from the studies. As an outcome of this review, it was proposed to develop a scientifically sound procedure for the exposure assessment of energy-saving bulbs, apply it to a selection of commercial bulbs, and then derive strategies that minimize the peak exposures. This report is the outcome of that proposal.

1.1 Light Bulb Technology

Until recently, the primary source of light used in homes has been incandescent light bulbs. The basic technology of incandescent lighting has been essentially unchanged since it was developed over 130 years ago. Incandescent bulbs generate light by simple blackbody radiation. A current is fed through a thin filament until the filament heats up to a high enough temperature (over 2500 °C) to emit radiation in the frequency range of visible light [7]. The heat that is produced by this process is wasted energy that results in their very low efficiency. The low efficiency of incandescent bulbs compared to that of ESBs is the reason why incandescent bulbs are increasingly being phased out in favour of more efficient light sources. Several countries have introduced legislation to phase out incandescent bulbs. Switzerland initiated a phase out program in 2009, with the complete phase out of bulbs that do not meet certain energy saving requirements by 2012.

ESBs have been designed to replace incandescent light bulbs. The principle of operation of an ESB can be described in three steps. The first step is the conversion of the 50 Hz signal to a higher frequency signal (typically 25 - 70 kHz) using an electronic ballast located at the base of the bulb. Conversion to a higher frequency eliminates light flicker and improves the efficiency of the bulb [8]. The second step is the excitation of mercury atoms in the tube by the higher frequency signal. Excited mercury atoms emit photons at ultraviolet frequencies (UV) which are not visible to the human eye. This requires a third step, which is the use of fluorescence to create visible light. A phosphor coating on the tube absorbs UV light and emits photons in the visible spectrum.

Light emitting diode (LED) bulbs are typically a single housing containing several individual LEDs. Each LED is a diode which when forward biased allows electrons to flow across a junction to combine with holes and release energy at visible frequencies. LED bulbs are relatively new compared to compact fluorescent ESBs. They are also more efficient than incandescent bulbs. This report investigates the three types of light bulb technology described in this section.

2 Safety Guidelines and Existing Standards

2.1 Safety Guidelines

Safety requirements for limiting exposure to time varying electric, magnetic and electromagnetic fields are enforced by regulations. At the international level, safety guidelines for EM exposure of workers/general public and controlled/uncontrolled environments have been issued by the International Commission on Non-Ionizing Radiation Protection (ICNIRP Guidelines, 1998 [9]) and the Institute of Electrical and Electronics Engineers (IEEE [10] and [11]). Their limits are given in Appendix A. The ICNIRP Guidelines form the basis for national regulations in many countries such as the countries of the EU. The legally enforced values in the USA are based on a mixture of the NCRP 1986 [12] and IEEE 1992 [13] guidelines. In addition, the EU issued a directive for workers, "EC 2004. Directive 2004/40/EC of the European Parliament and of the Council of 29 April 2004 on the minimum health and safety requirements regarding the exposure of workers to the risks arising from physical agents (electromagnetic fields) (18th individual Directive within the meaning of Article 16(1) of Directive 89/391/EEC)", based on the ICNIRP guidelines. Switzerland also adopted the ICNIRP guidelines but was the first country that introduced precautionary limits for sensitive areas that are 20 dB below the ICNIRP guidelines (NIS). These precautionary limits only apply for fixed installations.

The standards present limits for human exposure to electric fields, magnetic fields, and electromagnetic fields, and to induced and contact currents. They are defined to protect against health hazardous effects due to EM exposures. The recommendations are based on the review of the scientific data where only scientifically established adverse health effects have been considered, i.e., effects that have been independently confirmed by different laboratories.

2.1.1 Basic Restrictions

The basic restrictions refer to the induced fields inside the tissue on a macroscopic level. Therefore the predominant interaction mechanisms are different above and below 100 kHz, and thus the nature of and the rationale for the safety factors differ. Depending on the frequency, different scientific bases were used to develop exposure restrictions. Between 1 Hz and 10 MHz, basic restrictions are provided on current density to prevent effects on nervous system functions, such as aversive or painful electrostimulation. Between 100 kHz and 10 GHz, basic restrictions on SAR are provided to prevent whole-body heat stress and excessive localized tissue heating. In the 100 kHz-10 MHz range, restrictions are provided on both current density and SAR; and between 10 and 300 GHz, basic restrictions are provided on power density to prevent excessive heating in tissue at or near the body surface.

Exposure limitations are provided for the occupational exposed population or controlled and for the general public or uncontrolled. The occupational exposed population consists of adults who are generally exposed under known conditions and are trained to be aware of potential risks and take appropriate precautions. In contrast, the general public comprises individuals of all ages and of varying health statuses, and includes particularly susceptible groups or individuals.

The values for the basic limits, i.e., induced current density, whole-body and peal spatial SAR for the different standards are given in Appendix A.

2.1.2 Reference Level for Incident Field Strengths

Reference levels are derived for worst-case incident field strengths from the basic restrictions. The reference levels are given in Appendix A for International Commission on Non-Ionizing Radiation Protection (ICNIRP Guidelines, 1998 [9]) and the Institute of Electrical and Electronics Engineers (IEEE [10] and [11]).

2.1.3 Indirect Effects of Electromagnetic Fields

Indirect effects of electromagnetic fields may result from physical contact between objects at a different electric potential. In the frequency range of up to approximately 100 kHz, the flow from an object in the field to the body of the individual may result in the stimulation of muscles and/or peripheral nerves.

As the frequency increases from approximately 100 kHz to 10 MHz, the dominant effect changes from nerve and muscle stimulation to heating [14]. In this frequency range the threshold currents that produce perception and pain vary little as a function of the field frequency. The threshold of perception ranges from 25 to 40 mA in individuals of different sizes, and for pain from approximately 30 to 55 mA; above 50 mA there may be severe burns at the site of tissue contact. A summary about threshold currents for indirect effects based on the guidelines for limiting exposure to time-varying electric, magnetic, and electromagnetic fields (up to 300 GHz) given by the ICNIRP [9], are given in Appendix A. In general, it has been shown that the threshold currents that produce perception and pain vary little over the frequency range 100 kHz-1 MHz and are unlikely to vary significantly over the frequency range up to about 110 MHz.

2.2 Existing Measurement Standard

In addition to safety standards, product standards are developed to evaluate (by measurements or other means) the compliance of products with respect to these safety standards. For the evaluation of lighting equipment to the safety standards, standard IEC 62493 has recently been published [1]. This standard uses a measurement setup whereby a conducting sphere (210 ± 5 mm in diameter) is placed at a fixed distance (300 mm for ESBs) under a light source. The sphere is mounted on a non-conducting post so that it is electrically isolated from the ground. A voltage measured at the receiver is proportional to the electric and magnetic fields incident on the sphere, as described in the standard.

One limitation of this approach is that it does not measure the currents directly. The current density is calculated from the measured voltage using assumptions based on Faraday's law. Another limitation is that it is based on the incident fields on the metal sphere rather than the induced fields that could occur in the body. As shown in Figure 1, the presence of a person in the vicinity of a source in the kHz frequency range significantly alters the incident electric field distribution (the explanation of this setup is provided in Section 6.3.1). There is insufficient information in the standard to understand the rationale for using this setup or the correlation between the measured values and real human exposure under worst-case conditions. In reality, a person may be grounded, which may increase the currents flowing through the body.

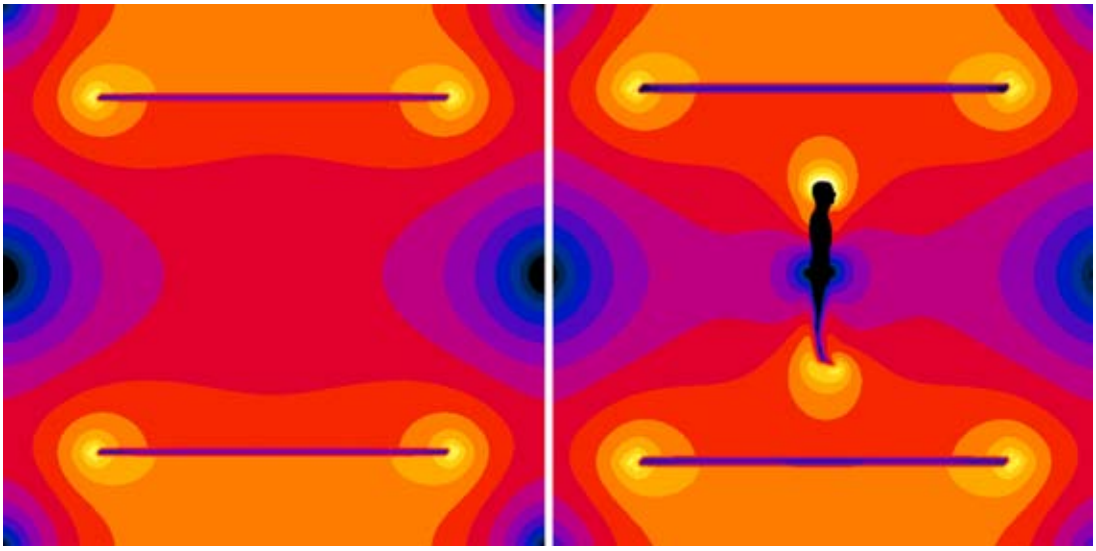

Figure 1: Electric field distribution in a parallel plate capacitor setup for two cases: without (left) and with (right) a human model placed in the center.

3 WP1 - Development of Test Conditions

3.1 Proposed Approach

This report proposes a novel method for determining the exposure of a person to the fields from energy saving bulbs. The exposure is assessed in terms of the induced fields in the body. The apparatus for the exposure measurements is described in this section. A conservative relationship between the current densities in the current density probe and the current densities in anatomical human models is developed.

3.2 Selection of Bulbs

The light bulbs selected for investigation are as follows: eleven ESBs (denoted E1 - E11 in this report), two incandescent bulbs (I1 and I2), two LED bulbs (L1 and L2) and two long fluorescent tube lights (T1 and T2). Please note that bulbs E3 and E4 are not sold in Switzerland at this time.

3.3 Selection of Lamps

To assess the fields from the bulbs in more realistic enviroments, three lamps were chosen as shown in Table 1. These lamps are representatives of a reading lamp, a bedside or table lamp and a standing lamp. To distinguish these lamps from bulbs, in this report, all ESBs, incandescent bulbs, long fluorescent tubes and LED lamps are referred to as 'bulbs' or 'lights' or 'tube lights'.

Table 1: Lamps selected for experimental assessment

Picture	Type	Remark
	Reading Lamp	Lamp shade and base are metallic (Adjustable height $\sim 0.7\,\mathrm{m}$)
	Bedside Lamp	Lamp with metallic base having a metallic wire frame to support the shade made out of cloth (Total height: $0.6\,\mathrm{m}$)
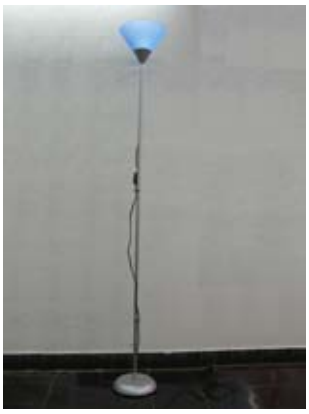	Standing Lamp	Lamp with metallic base having a plastic shade (Total height: $1.8\,\mathrm{m}$)

3.4 Measurement Setup

Measurements were conducted in a shielded enclosure to ensure that unwanted electromagnetic disturbances were eliminated. Using a metal enclosure also gives a well-controlled environment to measure the fields. The separation distance between the base of the bulb and the metal floor is 1200 mm. The bulb is centered in the metal enclosure, which has a length, width and height of 3700 ± 5 mm, 2200 ± 5 mm and 2600 ± 10 mm, respectively.

The measurement setup for the incident fields is shown in Figure 2. The incident fields are electric and magnetic fields measured in free space. The incident fields are measured at points where the geometric center of the sensor is located at the yellow and orange dots. Due to the size of the field probe, there are some locations that are too close to the bulb or apparatus to be measured.

The measurement setup for the induced fields is shown in Figure 3. The induced fields are quantified in terms of current densities measured in a lossy medium and compared with the basic restrictions of ICNIRP [9]. ICNIRP is in the process of revising its guidelines for frequencies from 1 Hz to 100 kHz, and a publicly-available draft [15] proposes to use induced electric field instead of current density as the basic restriction. The measurement setup of Figure 3 can also be used to measure the induced electric fields, since a simple relationship exists between the two quantities. The relevant distance for the current density measurements is the closest distance between the current density probe and the source. This distance is denoted d_J as shown in Figure 3. For the simulation results presented later, this distance is used to correlate the probe exposure to the exposure in the anatomical human models.

The apparatus used to position the probes is shown in Figure 4. The probe positioning apparatus is made of low loss and low permittivity materials (plexiglass, POM, and dry wood). Care has been made to minimize the amount and size of metal objects on the apparatus and inside the enclosure. An electric motor is used to rotate the bulb about its vertical axis. A second motor is used to move the probe to the correct position. The motors are always turned off during the measurements of the incident and induced fields.

The bulb is allowed to warm up and stabilize for at least 10 minutes before the measurements are started. To reduce fluctuations in the measurements and to capture the peak fields, the measurement software for the free-space probe is used in peak hold operation. For the induced current density measurements, data were captured over time (see Section 6.1) and post-processing was performed by following the ICNIRP guidelines given in [9].

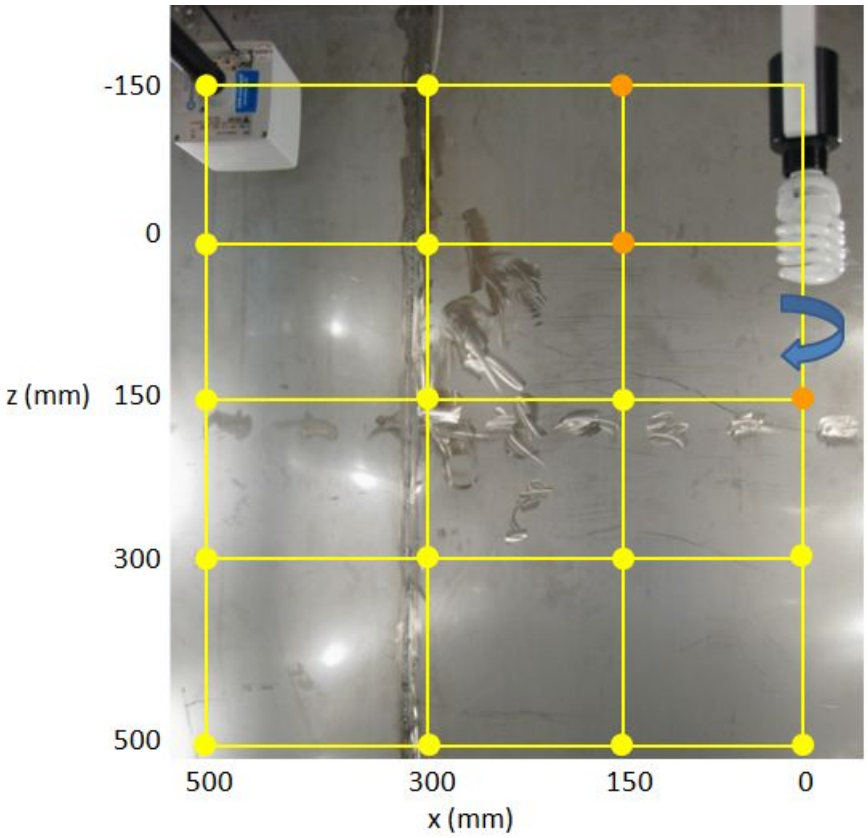

Figure 2: Measurement setup, showing the Narda EHP-200 probe (upper left) at a point on the grid (yellow lines) near the light bulb under test (upper right). The blue arrow shows the rotation of the bulb about its axis. The markings on the metallic wall behind the setup are polished areas that have no effect on the measurements.

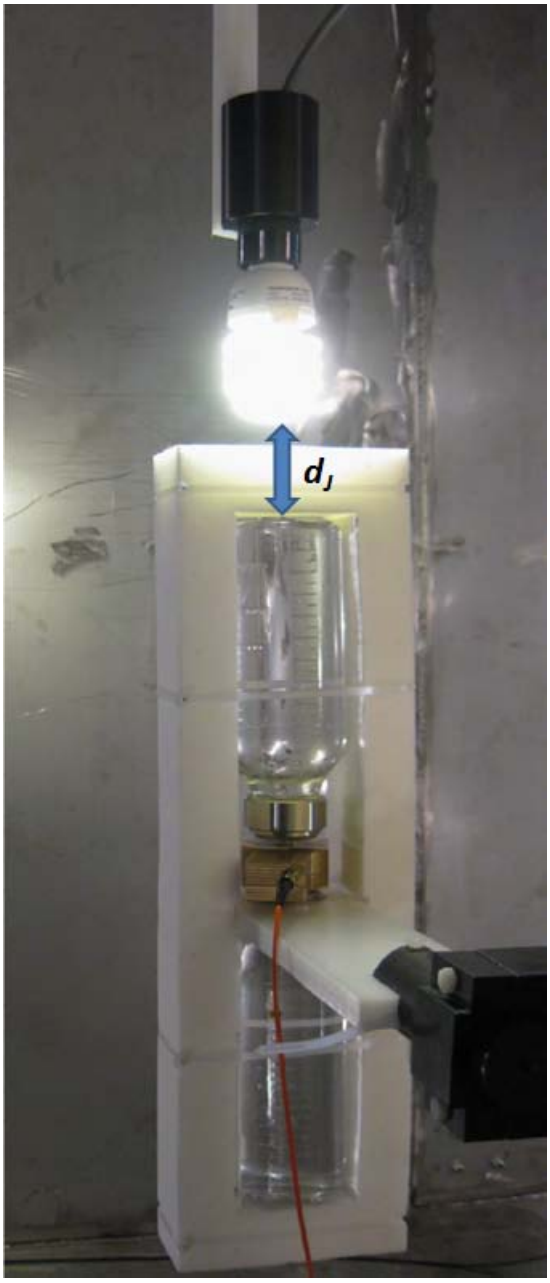

Figure 3: Measurement setup, showing the current density probe with the current clamp (gold colour). The distance used for current density measurements is denoted d_J, which is the shortest distance between the bulb and the current density probe, regardless of the orientation of the probe.

Figure 4: Measurement setup, showing the probe positioning apparatus as it positions the Narda EHP-200 probe under the light bulb.

4 WP2 - Instrumentation

Instrumentation has been developed and used to measure the exposure with respect to both basic restrictions and reference levels. The assessment of exposure with respect to the basic restrictions is performed using a current density probe. For the assessment of the exposure with respect to the reference levels of ICNIRP [9], a free-space E- & H-field probe is used. The probes and their specifications are detailed in the subsections below.

4.1 Incident Field Probes

For the measurement of the incident free-space electric and magnetic fields, a Narda EHP-200 probe is used (see Figure 5). The EHP-200 provides 3-axis measurements across the 9 kHz to 30 MHz frequency range. The measurement is converted to an optical signal at the probe, and the data are transmitted to the computer via an optical cable. The optical link is necessary so as not to disturb the electromagnetic fields in the environment. Software that is included with the probe enables the visualization of the frequency spectrum of the individual field components and total field. The software is used in peak hold operation, so that the highest rms field is measured. The specifications of the probe are given in Table 2.

Figure 5: Narda EHP-200 3-axis low frequency electric and magnetic field meter (source: http://www.narda-sts.de).

4.1.1 Noise Level

The noise level of the setup is shown in Figure 6 for the electric field and Figure 7 for the magnetic field. Both the equipment noise and the laboratory noise were measured.

The equipment noise level is the noise when all sources of EMF are turned off and the instrument should theoretically be measuring nothing (although imperfect shielding of the enclosure accounts for some noise).

The laboratory noise level quantifies the effect of other sources of electromagnetic fields in the laboratory, due to noise generated by the measurement equipment and other electromagnetic sources. These sources include incandescent lighting inside the enclosure and power lines leading into the enclosure. The laboratory noise level is the measured field when the light bulb source is turned off and the rest of the laboratory is operated normally as it is during the measurement of the light bulbs. The light bulb socket is powered on during the measurement.

At the frequency range of interest for the light bulb fields (25 — 70 kHz), the noise levels are less than 0.2 V/m for the electric field and 0.02 A/m for the magnetic field. Both noise levels are much less than 1% of the ICNIRP reference levels. The probe should be sufficiently sensitive for the measurements conducted for this report.

Table 2: Narda EHP200 specification (source: http://www.narda-sts.de).

RF Specification	Electric Field	Magnetic Field (mode A)
Frequency Range	9 kHz to 30 MHz	9 kHz to 30 MHz
Measurement Range @ 10 KHz RBW @ Preamp ON	 0.1 to 1000 V/m 0.02 to 200 V/m	 0.03 to 300 A/m 6.0 mA/m to 60 A/m
Dynamic Range	> 80 dB	> 80 dB
Sensitivity @ 10 kHz RBW @ Preamp ON	 0.1 V/m 0.02 V/m	 30 mA/m 6 mA/m
Resolution	0.01 V/m	1 mA/m
Flatness	± 0.5 dB (20 V/m, from 0.1 to 27 MHz)	± 0.8 dB (166 A/m, from 0.15 to 30 MHz)
Anisotropy	± 0.8 dB at 1 MHz	± 0.8 dB at 1 MHz
Linearity	0.5 dB @ 1 MHz from Full Scale to -60 dB Full Scale	
Typical Accuracy at 1 MHz	± 0.8 dB @ 20 V/m	± 0.8 dB @ 53 mA/m
Maximum Frequency Span	6 kHz to 30 MHz	6 kHz to 30 MHz
Resolution Bandwidths Available	1 kHz, 3 kHz, 10 kHz, 30 kHz, 100 kHz, 300 kHz	
Rejection to E-field		> 20 dB
Rejection to H-field	> 20 dB	
Temperature Error	0.02 dB / deg C	0.02 dB / deg C

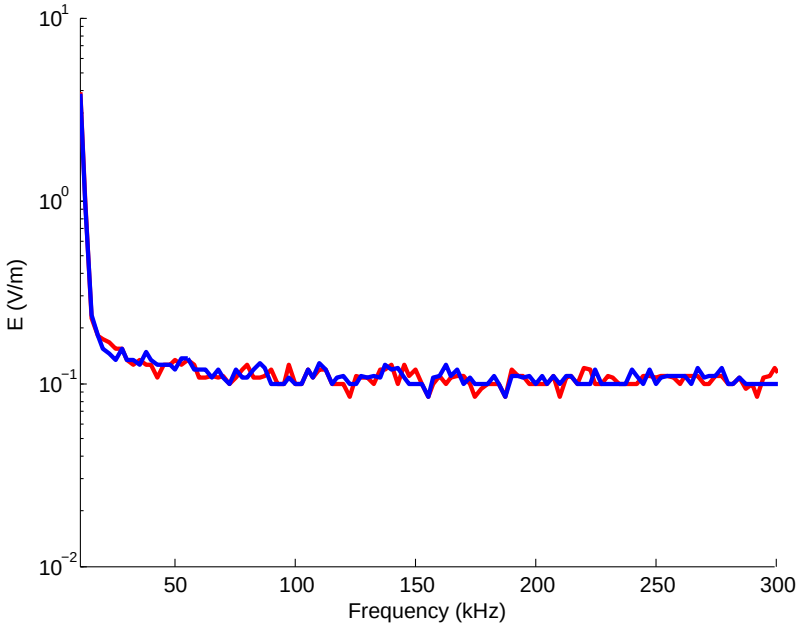

Figure 6: Noise level of the equipment (red) and the laboratory environment (blue) for the electric field.

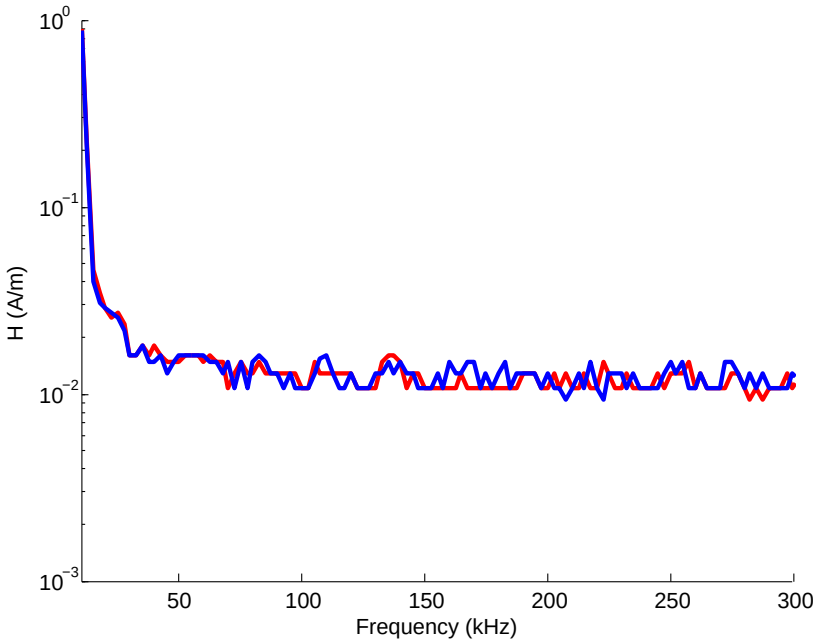

Figure 7: Noise level of the equipment (red) and the laboratory environment (blue) for the magnetic field.

4.2 *B*-field Narda Sensor ELT-400

50 Hz magnetic flux density (B-field) was measured using the Narda exposure level tester ELT-400 (see Figure 8).

Figure 8: Narda exposure level tester ELT-400.

The probe is especially designed for investigating the magnetic field produced by household equipment and other electrical devices. The reference test method described in EN50366 [16] is implemented in the Narda probe, and the measured B-field is given in [μT], or as a percentage of the ICNIRP guideline, 1998 [9]. The 3D-sensor system covers the frequency range 30 Hz to 400 kHz. The B-field is measured using three orthogonal coils with a common center point (allowing isotropic measurement). The cross sectional area is 100 cm^2 (standard-compliant), and the probe's external diameter is 125 mm. The signal voltages in the coils are digitized

and evaluated by a digital signal processor (DSP), which calculates in real-time the root-mean-square (rms) value of the B-field, according to EN50366 [16]. The rms-value of the magnetic flux density B is calculated from the rms-values of each of the three measurement axes (B_x, B_y and B_z) according to Equation (1).

$$B = \sqrt{B_x^2 + B_y^2 + B_z^2} \tag{1}$$

In this project, the Narda probe ELT-400 is used in *field strength mode*, which is a measurement of the magnetic flux density based on broadband evaluation of the signal, for the bandwidth 30 Hz to 400 kHz. This probe is primarily used to measure the 50 Hz B-field emanating from compact ESBs since the lowest frequency EHP-200 probe can measure is 9 kHz. The measurement uncertainty of the instrument is $\pm 4\,\%$ (50 Hz to 120 kHz). The frequency response for the selected bandwidth limits 30 Hz and 400 kHz is -3 dB ± 1 dB. The settings selected are given in Table 3. The intrinsic noise in the shielded chamber is 48 nT and 320 nT for the *low* and *high* range settings, respectively.

Table 3: Settings of the Narda probe ELT-400.

Mode	320 μT	
Range	Low	High
Overload Limit[a]	32 μT	320 μT
Nominal Measurement Range[b]	2 μT	20 μT
Intrinsic noise (rms)	48 nT	320 nT

[a] Maximum measurable rms-value of a sine wave.
[b] Maximum measurable rms-value of a signal of any shape with a crest factor (peak value/rms-value) of less than 22.

4.3 Clamp-on Current Probes

4.3.1 Introduction

A current probe is a clamp-on RF current transformer that determines the intensity of RF current present in an electrical conductor or group of conductors. Typical uses of these current probes is in the measurement of electromagnetic interference (EMI), in this case they are used in conjunction with EMI test receivers or spectrum analyzers. In evaluating EMI, the current clamp is used primarily with instruments having a 50-ohm input impedance. A current clamp probe provides a way to accurately measure net radio frequency current flowing on a wire or bundle of wires without requiring a direct connection to the conductor(s) of interest. The probe clamps around the test conductor which becomes a one turn primary winding; the probe forms the core and secondary winding of an RF transformer. Measurements can be made on single-conductor and multi-conductor cables, grounding and bonding straps, outer conductors of shielding conduits and coaxial cables, and so on.

This primary winding is considered as one turn since it is assumed that the noise currents flow through the conductor and return to the source by way of a ground conductor such as a frame, common ground plane, or earth. This is essentially the same as for induced currents in the human body, if a current clamp was placed over a limb it would provide the possibility to measure the total current induced in, e.g., a limb is the use of clamp-on current probes, Figure 9. A design for such a probe is presented in Blackwell, 1990 [17] and Hagmann, 1993 [18].

Some current probe models have the secondary output terminals resistively loaded internally such that they provide substantially constant transfer impedance over a wide frequency range.

This method of measuring the induced current has the advantage that sufficient sensitivity can be obtained by appropriate design of the test probe (increased current density at location of the probe) and the probe itself (e.g. number of coil windings, core material). A possible phantom design with a current probe is shown schematically in Figure 10. The phantom is filled with a saline and the probe is attached at the thinnest cylindrical section of it.

The performance of a current clamp is defined in terms of two primary quantities:

- the bandwidth - the frequency range over which the response is within 3 dB of the nominal value
- the transfer impedance - which relates the output voltage from the clamp to the current on the conductor.

Figure 9: Connectorised current clamps (left) and an optically linked induced current meter (right) (source: http://www.ets-lindgren.com/).

4.3.2 Optical Current Clamp Design

Commercial current clamps intended for EMI usage are designed for use in 50 Ω systems and typically have very low transfer impedances which limits the overall sensitivity and require a coaxial to connect the current clamp to the measurement equipment. For the measurements intended in this project the coaxial cable will potentially disturb the incident field on the measurement probe influencing the measurement itself. Where the current clamp has an optical link (connection is transparent to incident fields) such as in ETS-Lindgren's Model HI-3702, the device only measures the total current and does not provide information on the spectral content of the induced currents. For this reason an optically linked high sensitivity current clamp that could provide full details of the spectrum of induced currents was developed within the project and fully characterized.

The heart of the current clamp is a toroidal core made from a ferrite magnetic material, this acts as the core for the current transformer. There are many different types of ferrite material with different nominal frequency ranges. A material was chosen that is optimized for the frequency range 1kHz to 1 MHz for pulse transformer and 0.5 to 20 MHz in wide band transformers. In the case of a current clamp the primary circuit with the current to be measured

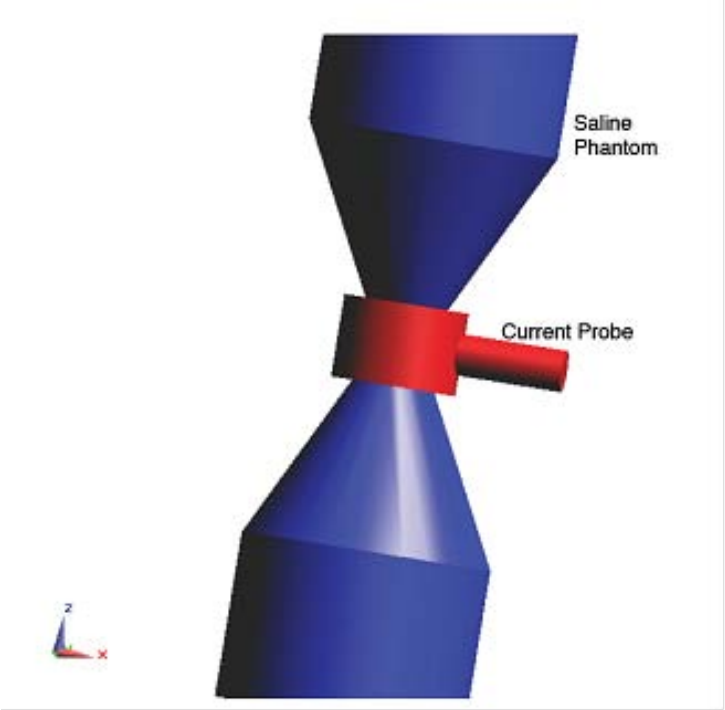

Figure 10: Saline phantom with current probe.

passes through the centre of the current clamp and forms the equivalent of one turn ($n_1 = 1$). The number of turns in the secondary n_2 can be altered to provide the best trade off between low frequency cut-off and transimpedance. The low frequency cut-off is proportional to $(n_1/n_2)^2$ and the transimpedance to $\sqrt{n_2/n_1}$ and both are a function of the load resistance.

For this application to improve the sensitivity the load resistance was chosen to be 1000Ω and with a turns ratio of 28 the low frequency cut-off was maintained at 25 kHz. The probe is usable with reduced sensitivity down to 5 kHz.

The output signal from the current clamp is amplified using a wideband operational amplifier configured to present a constant resistive load of 1 kΩ to the clamp and have a voltage gain of 10. This signal then linearly modulates a Honeywell VCSEL laser with the time domain signal from the current clamp. In Figure 11 it can be seen that when the laser is biased at between 10 and 15 mA the voltage - current relationship is linear and the output power will be a direct function of the drive voltage from the op-amp. The laser diode is biased using a simple current mirror and current reference. The whole current clamp, optical transmitter and battery are housed in a shielded enclosure, this enclosure has a split in the shield in side the toroid such that it provides an electrostatic shield but does not form a shorted turn in the transformer. A block diagram can be seen in Figure 12 and the completed current clamp can be seen in Figure 13.

The optical receiver consists of an AC coupled reverse biased PIN diode followed by a transimpedance amplifier based on a wide band operational amplifier with a transfer impedance of 1 kΩ. This has a low output impedance and can drive an oscilloscope or a spectrum analyzer. In our case the signal was sampled using a digital oscilloscope and the spectrum computed using a fast Fourier transform.

After completion of the optical current clamp it was characterized in the laboratory and calibration data produced. A 50 Ω source was connected to a 50 Ω load inserted through the current clamp and the voltage across the 50 Ω is monitored to allow calculation of the current, Figure 14. The return loss of the 50 Ω load was measured across the entire frequency range to

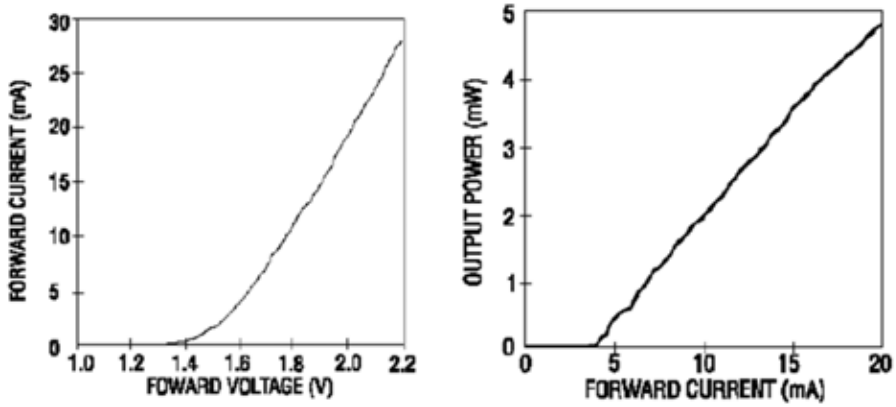

Figure 11: VCSEL laser current as a function of voltage and output power as a function current.

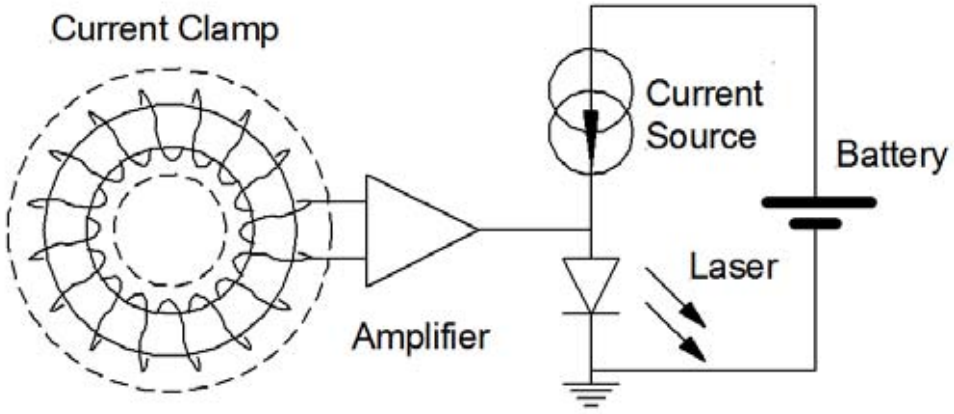

Figure 12: Block diagram of the optical current source.

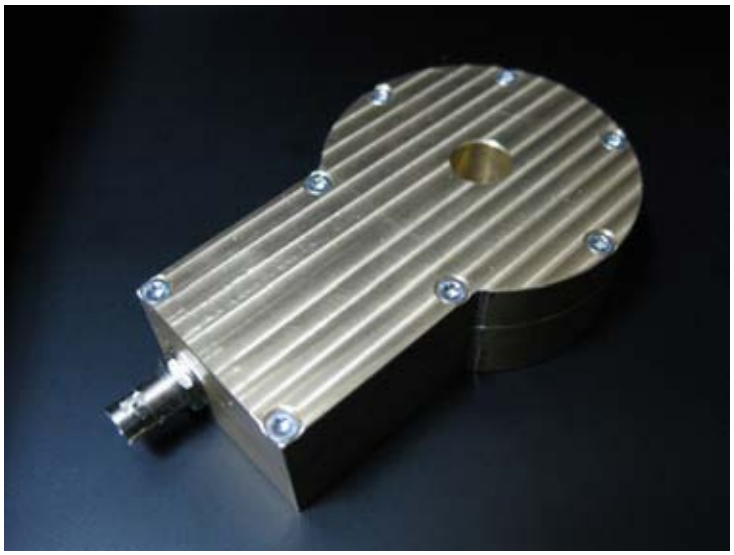

Figure 13: Optical current clamp.

ensure that is was within reasonable limits (return loss > 30 dB). The frequency of the source was swept over the frequency range and the input and output voltages measured at each frequency. The calibration factor (transimpedance) was then calculated for the whole measurement system.

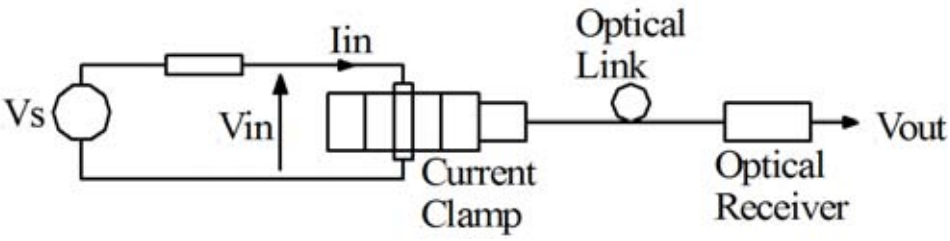

Figure 14: Calibration Setup.

The resultant transfer impedance can be seen in Figure 15 and Figure 16 and these data are used to postprocess the measured results to convert the voltage spectrums measured to the equivalent spectrum of the induced current in the current density probe.

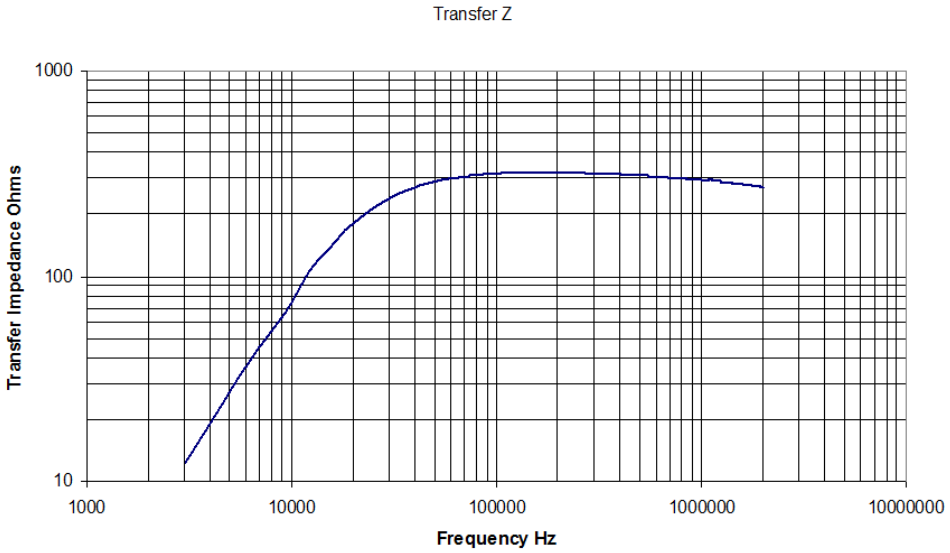

Figure 15: Optical current clamp transfer impedance.

4.4 Saline Phantom

To measure the induced current densities, the authors adopted the measurement concept that SPEAG and IT'IS jointly developed for another project conducted for KABA. The concept implementation is described below.

At frequencies below 10 MHz, external electromagnetic fields induce currents in the body. To estimate the currents induced in a person, liquid-filled phantoms have been developed. The purpose of the phantom is to represent the dominant mechanism of induced fields in a person while being relatively easy to build and maintain. Two phantoms have been developed for this purpose: a linear phantom to measure the current density from the incident electric field (Figure 17) and a loop phantom to measure the current density from the incident magnetic field. As discussed in Section 5, the loop phantom was not needed, as the electric fields dominate the magnetic fields for all bulbs investigated.

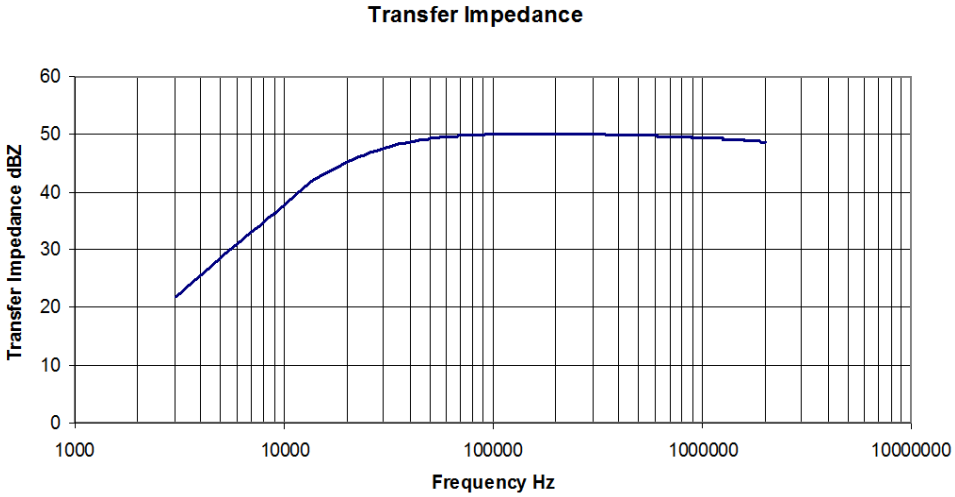

Figure 16: Optical current clamp transfer impedance in decibels relative to 1 Ω.

The linear phantom consists of two cylindrical bottles connected on either end of a metal component. The bottles are made of a polycarbonate material. Due to the small thickness of the plastic (approximately 1 mm) and the low relative permittivity (ϵ_r between 3 and 4.5 at 1 MHz [19]) compared to saline, the plastic material is considered to be invisible to fields at frequencies less than 1 MHz. Each bottle has an outer diameter of 74 mm and a height of 180 mm. The outer diameter tapers at the neck to 40 mm. The neck of the bottle is fitted with a silicone seal ring, and each connector of the metal component fits over the seal to contain the saline in the phantom.

The metal component consists of a cylindrical rod between two connectors. The cylindrical rod has a length of 50 mm and a diameter of 8 mm. The connectors have inner and outer diameters of 40 mm and 50 mm, respectively. The total size of the phantom, including the two bottles and the metal component, is 74 mm × 74 mm × 420 mm.

The bottles are filled with a 0.01 M saline solution. This particular saline concentration was chosen because its conductivity is similar to the average conductivity for white matter (0.0818 S/m) and grey matter (0.1337 S/m) of the human brain at 100 kHz [20]. The relative permittivity and conductivity of 0.01 M saline are 80.14 and 0.094 S/m at 100 kHz. A saline recipe was mixed in the laboratory using 0.561 grams of NaCl per 1 liter of de-ionized water (having conductivity of 50 μS/m). The molarity of the saline mixture was verified by measuring its dielectric parameters using an open-coaxial probe technique [21]. The Agilent 85070C dielectric probe kit was used. This probe has a measurement uncertainty typically within 5% at frequencies above 200 MHz. It is not suitable for measurements in the frequency range of 30 — 100 kHz, due to noise and electrode polarization effects [20]. Therefore, the dielectric parameters were measured at higher frequencies to verify the saline concentration. At a frequency of 2 GHz, the agreement between the measurements and the published values was found to be within 0.5% for permittivity and 2% for conductivity.

4.4.1 Noise Level

The noise levels are shown in Figure 18 for the current density equipment and the laboratory environment. The equipment noise level and laboratory noise level were described in Section 4.1.1.

At the frequency range of interest for the light bulb fields (20 — 300 kHz), both the equipment and laboratory noise levels are less than 0.02 mA/m^2. These noise levels are much less than 1%

Figure 17: Linear saline phantom with current clamp (gold color). Current clamp is located between the two cylindrical bottles.

of the ICNIRP basic restriction, which is $60\,\mathrm{mA/m^2}$ at 30 kHz. It can therefore be concluded that the equipment is sufficiently sensitive for the current density measurements conducted for this report.

4.5 Numerical Method

4.5.1 Finite-Difference Time-Domain Method

The finite-difference time-domain (FDTD) method is used for the numerical evaluation of the exposure [22]. The FDTD method calculates E- and H-field vectors at all locations of the computational space. The vector components of the field are located on a rectilinear grid with an offset of half a mesh step between the E- and the H-fields. This arrangement of the field components permits the straightforward approximation of Maxwell's equations in a second order finite difference form. Simulations are carried out in the time-domain. E- and H-fields are updated based on their previous values using a fixed time step. In this manner, electromagnetic waves can propagate in the computational domain. For stable operation, the time step is limited by the Courant-Friedrichs-Lewy criterium [23]. Its value depends on the size of the smallest cell in the mesh.

The mesh resolution is determined by the maximum permissible numerical dispersion error [24] or the geometrical characteristics of the geometry to be modeled. Correctly rendering the exposure source and the human body models requires mesh step sizes in the order of magnitude of 1 mm — 5 mm, which leads to negligible numerical dispersion.

The FDTD method is particularly well suited for the simulation of anatomical models because complex tissue distributions can be directly rendered on the computational grid. The local dielectric properties can directly be assigned to finite difference equation which operates on

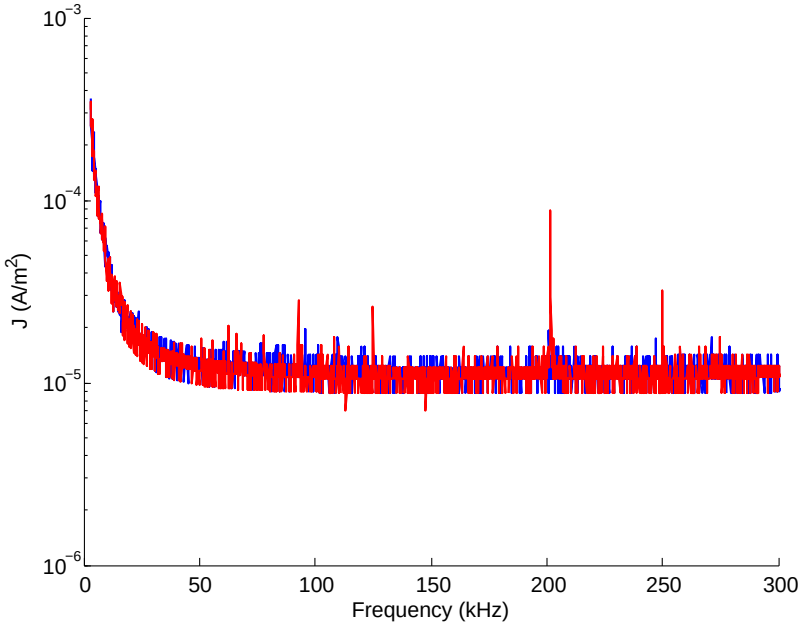

Figure 18: Noise level of the current density equipment (red) and the laboratory environment (blue).

the respective grid edge. For all simulations, the integrated simulation platform SEMCAD X (Schmid & Partner Engineering AG, Zürich) is used. SEMCAD X combines a flexible CAD modeling environment with a highly efficient FDTD kernel and a post processor for the extraction of all required quantities, such as SAR averaging according to [25].

4.5.2 Anatomical Models

Conventional dosimetric models of the human body consist of prevoxeled data of a fixed resolution. In numerical simulations using the FDTD method, this generally determines their orientation in the computational grid as well as the mesh resolution. If the models need to be rotated in the computational domain, or if their resolution must be modified due to numerical reasons, this usually goes along with loss of accuracy due to multiple sampling, particularly with respect to small organs or thin tissue layers, such as the skin.

In order to overcome these disadvantages, nine whole body models (two male adults, one adult female (not pregnant and in three gestational phases) and six children) were developed within the framework of the Virtual Family Project [26] and several follow up studies. The models are based on high resolution MRI scans (0.5 mm×0.5 mm×1.0 mm in the head, 0.9 mm × 0.9 mm× 2 mm in the trunk and the limbs) using a Siemens Avanto 1.5 T scanner. More than 80 tissues and organs were segmented using an in-house software and reconstructed as three-dimensional CAD objects yielding anatomical models of unprecedented fidelity and quality. These models can be arbitrarily placed in the grid and meshed at arbitrary resolution without loss of detail.

Figure 19 shows the four CAD models used for the simulations of this study: a male and a female adult, an eleven year old girl and a six year old boy. Table 4 summarizes their anatomical characteristics. Currently, additional software is under development, which allows the natural articulation of the limbs of the models [27].

Name	Age [years]	Sex	Height [m]	Weight [kg]	BMI [kg/m^2]
Duke	34	male	1.74	70	23.1
Ella	26	female	1.60	58	22.7
Billie	11	female	1.46	36	16.7
Thelonious	6	male	1.17	20	14.2

Table 4: Characteristics of the four anatomical models.

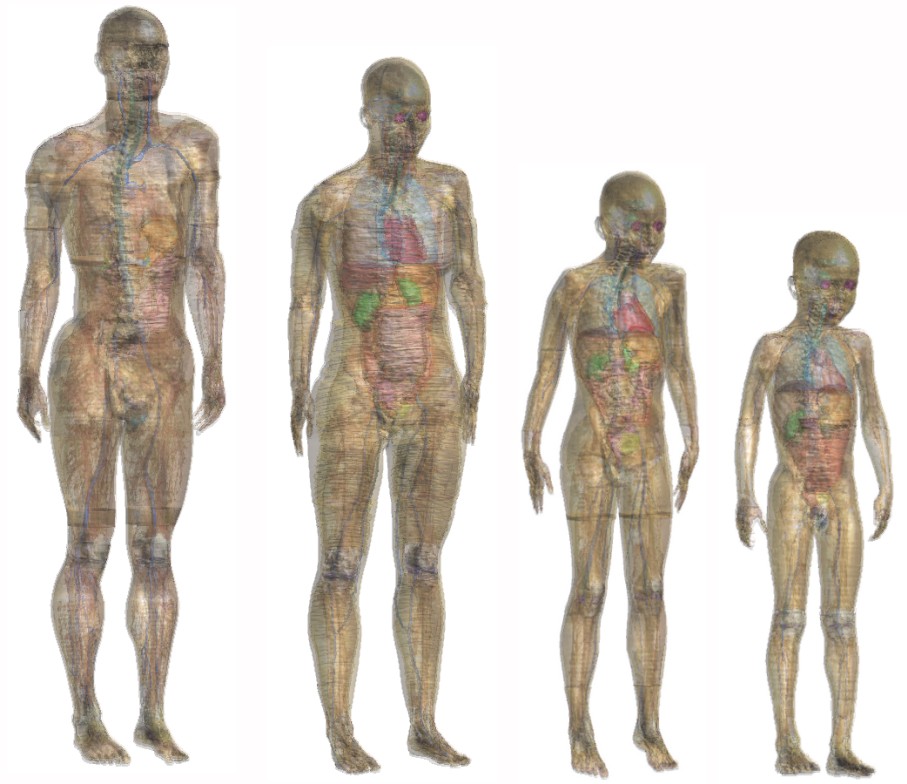

Figure 19: Anatomical whole body models (from left to right): Duke, Ella, Billie, Thelonious (Table 4).

4.6 Low Frequency Solver

4.6.1 Introduction

The well known Maxwell's curl equations describe the physics of electromagnetic field propagation. The equations can be transformed into frequency domain by assuming a harmonic oscillation $\exp j\omega t$ where j is the complex number with $j^2 = -1$, ω is the angular frequency $\omega = 2\pi f$, and t denotes the time.

Maxwell's equations can be written in frequency domain ($\vec{X}(\vec{r},t) = \Re(e^{j\omega t}\mathbf{X}(\vec{r}))$, i.e., $\mathbf{X}$ is a complex valued vector (phasor), ω the angular frequency and $\partial/\partial t \equiv j\omega$) as follows:

$$\nabla \times \mathbf{E} = -j\omega\mathbf{B} \tag{2a}$$

$$\nabla \times \mathbf{H} = j\omega\mathbf{D} + \mathbf{J} \tag{2b}$$

$$\nabla \cdot \mathbf{D} = \rho \tag{2c}$$

$$\nabla \cdot \mathbf{B} = 0 \tag{2d}$$

where $\mathbf{E}$, $\mathbf{D}$, $\mathbf{B}$, $\mathbf{H}$, and $\mathbf{J}$ are the phasors of the electric field, displacement current, magnetic flux,

magnetic field, and the current density field, respectively. The charge distribution is denoted as ρ. A direct consequence of equations (2b) and (2c) is the charge continuity equation

$$\nabla \cdot \mathbf{J} + j\omega\rho = 0. \tag{3}$$

In addition, the constitutive laws hold for linear materials

$$\mathbf{D} = \epsilon\mathbf{E} \tag{4a}$$
$$\mathbf{B} = \mu\mathbf{H} \tag{4b}$$
$$\mathbf{J} = \sigma\mathbf{E} + \mathbf{j_0} \tag{4c}$$

where $\epsilon := \epsilon_0\epsilon_r$ is the electric permittivity, $\mu := \mu_0\mu_r$ is the magnetic permeability. The Ohmic losses are denoted by the electric conductivity σ and the source current is $\mathbf{j_0}$. Last but not least, the complex permittivity $\tilde{\epsilon}$ is defined as $\tilde{\epsilon} := \epsilon_r\epsilon_0 + \frac{\sigma}{j\omega}$.

4.6.2 Decouple Magnetic from Electric Field

Introducing the vector potential $\mathbf{A}$ with $\nabla \times \mathbf{A} = \mathbf{B}$ (in Coulomb gauge, i.e., $\nabla \cdot \mathbf{A} = 0$), solves equation (2a) and (2d) and determines the electric field $\mathbf{E}$ up to a curl-free part (Helmholtz decomposition):

$$\mathbf{E} = \underbrace{-j\omega\mathbf{A}}_{:=\mathbf{E}_s} + \underbrace{\nabla\phi}_{:=\mathbf{E}_i} = \mathbf{E}_s + \mathbf{E}_i \tag{5}$$

where ϕ is a scalar potential and $\nabla \cdot \mathbf{E}_s = j\omega\nabla \cdot \mathbf{A} = 0$ (solenoidal), $\nabla \times \mathbf{E}_i = \nabla \times \nabla\phi = 0$ (irrotational). Writing equation (2b) with the new potentials gives

$$\nabla \times \frac{1}{\mu}\nabla \times \mathbf{A} = \omega^2\tilde{\epsilon}\mathbf{A} + j\omega\tilde{\epsilon}\nabla\phi + \mathbf{j_0} \tag{6}$$

and charge continuity equation (3) becomes

$$\nabla \cdot \tilde{\epsilon}\nabla\phi = j\omega\nabla \cdot \tilde{\epsilon}\mathbf{A} \tag{7}$$

when we assume, that no charges are generated ($\nabla \cdot \mathbf{j_0} = 0$), e.g., we have closed current loops. With unknown charge distribution ρ, the remaining equation (2c) is a 'left over' equation to determine ρ. Therefore, equation (2c) is not used to calculate the potentials.

4.6.3 Quasi-Static Approximation

Investigating each term in the continuity (7) reveal the following scaling property

$$\nabla \cdot \tilde{\epsilon}\nabla\phi\text{-term} = \mathcal{O}(\tilde{\epsilon}\phi/l_\phi^2) \tag{8a}$$
$$\nabla \cdot \omega\tilde{\epsilon}\mathbf{A}\text{-term} = \mathcal{O}(\omega\tilde{\epsilon}A/l_A) \tag{8b}$$
$$\tag{8c}$$

where $\mathcal{O}(\cdot)$ denotes the 'in the order of' symbol, e.g.,

$$\mathcal{O}(x^3) : \lim_{x\to 0} \frac{\text{term}}{x^3} = const, \tag{9}$$

and l_A and l_ϕ are characteristic lengths and $\mathcal{O}(1/l)$ is the scaling of a derivative. Therefore, the scaling of the ϕ magnitude can be derived from the scaling property (8) and is

$$\phi = \mathcal{O}(\omega A l_\phi^2/l_A). \tag{10}$$

Using the same strategy on equation (6) yields

$$\nabla \times \frac{1}{\mu} \nabla \times \mathbf{A}\text{-term} = \mathcal{O}(A/\mu l_A^2) \tag{11a}$$

$$\omega^2 \tilde{\epsilon} \mathbf{A}\text{-term} = \mathcal{O}(\omega^2 \tilde{\epsilon} A) \tag{11b}$$

$$j\omega\tilde{\epsilon}\nabla\phi\text{-term} = \mathcal{O}(\omega\tilde{\epsilon}\phi/l_\phi) \overset{(10)}{=} \mathcal{O}(\omega^2\tilde{\epsilon}Al_\phi/l_A) \tag{11c}$$

Therefore, the terms (11b) and (11c) can be compared to the $\nabla \times \nabla \times$ -term (11a):

$$\frac{\omega^2 \tilde{\epsilon} \mathbf{A}\text{-term}}{\nabla \times \frac{1}{\mu} \nabla \times \mathbf{A}\text{-term}} = \mathcal{O}(\omega^2 \tilde{\epsilon} \mu l_A^2) = \mathcal{O}\left(\left(\frac{l_A}{\lambda}\right)^2\right) \tag{12a}$$

$$\frac{j\omega\tilde{\epsilon}\nabla\phi\text{-term}}{\nabla \times \frac{1}{\mu} \nabla \times \mathbf{A}\text{-term}} = \mathcal{O}(\omega^2 \tilde{\epsilon} \mu l_A l_\phi) = \mathcal{O}\left(\frac{l_A l_\phi}{\lambda^2}\right) \tag{12b}$$

The term $\omega^2\tilde{\epsilon}\mu$ is equivalent to k^2, where k is the wavenumber $k = 2\pi/\lambda$ and λ is the wavelength. Therefore, the term scales like $\mathcal{O}(1/\lambda^2)$. Hence, we can neglect the two terms (12) in equation (6) (if all cells and materials satisfy the condition), if

$$|\omega^2 \tilde{\epsilon} \mu d^2| \ll 1 \qquad \Longleftrightarrow \qquad \left(\frac{d}{\lambda}\right)^2 \ll 1 \tag{13}$$

or written as real-valued criteria

$$\omega^2 \epsilon \mu d^2 \ll 1 \tag{14a}$$

$$\omega \sigma \mu d^2 \ll 1 \tag{14b}$$

where d is the worst case, i.e., the diameter of the computational domain, and equations (6) reduces to

$$\nabla \times \frac{1}{\mu} \nabla \times \mathbf{A} = \mathbf{j_0}, \tag{15}$$

i.e., the vector potential $\mathbf{A}$ is the magneto static vector potential $\mathbf{A}_0$ and is completely decoupled from the electric field $\mathbf{E}$. If in addition $\mu \equiv \mu_0$ is constant[1] over the whole domain Ω, $\mathbf{A}_0$ is calculated by the law of Biot-Savart

$$\mathbf{A}_0(\vec{r}) = \frac{\mu_0}{4\pi} \int_\Omega \frac{\mathbf{j_0}(\vec{r}')}{|\vec{r} - \vec{r}'|} d\vec{r}'. \tag{16}$$

4.6.4 Choosing the Appropriate LF Solver

If conditions (14a) and (14b) are fulfilled for a suitable characteristic length, the following quasi-static approximation models can be derived:

- $\mathbf{j_0} \equiv \mathbf{0}$: From equation (15) or (16) we can learn, that the vector potential vanishes, i.e., $\mathbf{A}_0 \equiv \mathbf{0}$. Therefore, the electric field only consists of the scalar potential ϕ. Using equation (7), we get

  $$\nabla \cdot \tilde{\epsilon} \nabla \phi = 0, \qquad \text{Electro Quasi-Static (E-QS)} \tag{17}$$

  'excited' by boundary conditions, i.e., specifying potential values. The electric field $\mathbf{E}$ is calculated by applying the gradient operator $\mathbf{E} = \nabla\phi$. This complex valued equation

[1] Of course, any constant μ_r is valid as well. For simplicity, the constant is still called μ_0.

might be further simplified, when the condition holds for all materials in the computational domain:

$$\sigma \ll \omega\epsilon: \quad \nabla \cdot \epsilon\nabla\phi = 0, \qquad \text{Electro Static} \tag{18}$$

$$\sigma \gg \omega\epsilon: \quad \nabla \cdot \sigma\nabla\phi = 0, \qquad \text{Stationary Currents} \tag{19}$$

The models (18) and (19) are independent from the specified frequency, i.e., the same ϵ or σ distribution yields the same result. However, the conditions (14a) and (14b) change, i.e., the approximation accuracy changes.

- $\mathbf{j_0} \neq \mathbf{0}$: From equation (15) we learn, that the vector potential is the magneto static vector potential $\mathbf{A}_0$ 'excited' by the current distribution $\mathbf{j_0}$. Therefore, $\mathbf{A}_0$ is calculated by solving the magneto static problem (15) or if $\mu \equiv \mu_0, \text{in}\,\Omega$ by integrating Biot-Savart (16). Then, the $\mathbf{E}$ field is determined by the following strategy. Using again equation (7) and the fact that $\nabla \cdot \mathbf{j_0} = 0$ (closed current loops), we yield

$$\nabla \cdot \tilde{\epsilon}\nabla\phi = j\omega\nabla \cdot (\tilde{\epsilon}\mathbf{A}_0), \qquad \text{Magneto Quasi-Static (M-QS).} \tag{20}$$

The total electric field $\mathbf{E}$ is calculated with equation (5). Again, this complex valued equation might be further simplified, when the condition holds for all materials in the computational domain:

$$\sigma \ll \omega\epsilon: \quad \nabla \cdot \epsilon\nabla\phi = j\omega\nabla \cdot (\epsilon\mathbf{A}_0), \qquad \text{M-QS: Displ. current dom.} \tag{21}$$

$$\sigma \gg \omega\epsilon: \quad \nabla \cdot \sigma\nabla\phi = j\omega\nabla \cdot (\sigma\mathbf{A}_0), \qquad \text{M-QS: Ohmic current dom.} \tag{22}$$

4.6.5 Implemented Methods in *SEMCAD X*

The following quasi-static models of subsection 4.6.4 are implemented in the current *SEMCAD X* Bernina version. A short description of valid boundary conditions and grid settings is provided in addition.

Electro Static Equation (18) is implemented. Aside from purely electro static simulations, this model can be used to analyze simulation scenarios if all solid regions fulfill the condition in (18). This model uses the real-valued solver `LFSolver`. Dirichlet (fixed potential value) or Neumann (vanishing flux normal to the computational boundary) are available for this model. Open boundary conditions have to be approximated by a large padding and Dirichlet or Neumann boundary conditions.

Stationary Currents, Electro QS Ohmic Current Dominated Equation (19) is implemented. The $\mathbf{E}$ field is only calculated in the lossy ($\sigma \neq 0$) domain whereas the $\mathbf{H}$ field is calculated overall. Therefore, the default grid covers only the lossy domain. Despite its naming, this model can be used in electro quasi-static simulations, when the ohmic current dominates the displacement current. At the interface lossy – non-lossy vanishing flux interface conditions are applied. Dirichlet (fixed potential value) or Neumann (vanishing flux normal to the computational boundary) are available for this model. This model uses the real-valued solver `LFSolver`.

Electro Quasi-Static Equation (17) is implemented. This model uses the complex-valued solver `LFSolver`. Dirichlet (fixed potential value) or Neumann (vanishing flux normal to the computational boundary) are available for this model. Open boundary conditions have to be approximated by a large padding and Dirichlet or Neumann boundary conditions.

Magneto Quasi-Static (Biot-Savart) Equation (22) is implemented. All boundary conditions are neglected, i.e., are zero Neumann boundary conditions (vanishing normal flux). The LF current sources cannot be part of the *lossy* computational domain, due to field singularity reasons. This model uses the real-valued solver `LFSolver`. The **E** field is only calculated in the lossy ($\sigma \neq 0$) domain whereas the **H** field is calculated overall. Therefore, the default grid covers only the lossy domain.

Magneto Static (Biot-Savart) Equation (16) is implemented. Because the model assumes constant permeability, all solid regions are neglected and only the LF current sources are considered. The background solid region defines the used permeability. All boundary conditions are neglected. The LF current sources may or may not be part of the computational domain. This model uses the complex-valued solver `LFSolver`.

All LF models display in the message window and write in the log file a table the quasi-static approximation criteria.

5 WP3 - Assessment of the Incident Fields

5.1 9 kHz to 1 MHz Electric and Magnetic Fields

The incident electric and magnetic fields were measured for the selected light bulbs using the Narda EHP-200 probe described previously (Figure 5). Table 5 shows the total electric and magnetic field directly below each of the light bulbs. These readings were recorded with a resolution bandwidth of 10 kHz and with the detector setting on peak hold for about 30 seconds to ensure that the maximum value was reached and also to reduce fluctuations in measurements. The probe was placed such that its geometric center is 150 mm directly below the center point of the light source. The probe was moved as needed to maintain this distance, which depends on the length of the bulb. The measured fields are given both in absolute terms and with reference to the appropriate ICNIRP reference levels for general public exposure. The reference levels are 87 V/m for the electric field and 5 A/m for the magnetic field.

It can be seen that the magnetic field is very low in comparison to the electric field, with values of 2 % or less of the ICNIRP reference levels. The electric field is much higher in magnitude, particularly for the ESBs, and the magnitude is strongly dependent on the type of bulb. In fact, the ICNIRP reference level is exceeded for most of the ESBs at this distance. The magnetic field is relatively low for ESBs due to the symmetrical construction of the fluorescent tubes which allows for currents to cancel each other. It is possible that ESBs with different tube geometries could have higher magnetic fields than those reported here. It can be observed that the ESBs with a spiral (double helix) tube design generally have lower H fields than ESBs with a folded or stick tube design.

The electric field values for the incandescent and LED bulbs are very low.

Table 6 shows the same result as the previous table, but at a distance of 300 mm. It is observed that the values are significantly lower at this distance. All values are below the ICNIRP reference values for general public exposure. The magnetic field levels are in the range of the noise level for this probe. These results show that the electric field is the relevant exposure quantity. For the rest of this report, only the electric field will be assessed at frequencies in the kHz range.

Figure 20 shows a 3-dimensional representation of the total electric field surrounding the E4 bulb, which has the highest electric field value in Table 5. The total electric field was measured in five planes. The closest distance between the center of probe and the center of bulb is 120 mm. The plots are in dB(V/m) scale in order to more easily visualize the distributions. The highest value measured was 54.7 dB(V/m), or 543 V/m in linear scale. This value is considerably above the ICNIRP reference level of 87 V/m at this very close distance. The field decays rapidly (stronger than exponential) as the distance increases away from the bulb. At a distance of 300 mm from the center of the bulb, all of the electric field values are below the ICNIRP reference levels.

Figure 21 shows the three electric field components and the total electric field in the plane containing the axis of the bulb. This slice corresponds to the measurement grid of Figure 2. The measured data have been interpolated to a 1 mm resolution. The blue rectangle in the upper right of each figure represents the area where the probe was too close to the apparatus to perform a measurement. The figures show that the electric field is emanating radially away from the bulb. The highest value for the E_z (vertical) component is found directly under the bulb, where the fields are eminating vertically towards the ground, whereas the highest value for the E_x (horizontal) component is found directly beside the bulb, where the fields are radiating horizontally away from the bulb. The E_y component (direction into the page) is very low compared to the other two components.

As discussed earlier, the reference levels are derived from the basic restrictions under worst-case assumptions. ICNIRP allows the reference levels to be exceeded as long as the basic restrictions are obeyed. Section 6 addresses the measurement of the current density against the

Bulb	E_{total} (V/m) rms	% of ICNIRP limit	H_{total} (A/m) rms	% of ICNIRP limit	f_0 (kHz)
ESBs					
E1	68.2	78.4 %	0.016*	< 0.5 %	50
E2	102	118 %	0.018*	< 0.5 %	45
E3	98.2	113 %	0.016*	< 0.5 %	45
E4	433	497 %	0.020*	< 0.5 %	50
E5	143	165 %	0.083	1.7 %	42.5
E6	92.1	106 %	0.086	1.7 %	40
E7	139	160 %	0.073	1.5 %	55
E8	76.6	88.0 %	0.016*	< 0.5 %	47.5
E9	74.5	85.6 %	0.098	2.0 %	25
E10	71.8	82.5 %	0.016*	< 0.5 %	45
E11	115	132 %	0.105	2.1 %	40
Incandescent Bulbs					
I1	0.58	0.7 %	0.015*	< 0.5 %	67.5
I2	0.58	0.7 %	0.015*	< 0.5 %	67.5
LED Bulbs					
L1	0.63	0.7 %	0.018*	< 0.5 %	40
L2	2.8	3.3 %	0.038	0.8 %	65
Noise Floor	0.13		0.015		

* Measurement is below twice the noise level of Narda EHP-200 probe (see Figures 6 and 7).

Table 5: Total electric and magnetic fields directly below the light bulb at a center-to-center distance of 150 mm.

basic restrictions.

Bulb	E_{total} (V/m) rms	% of ICNIRP limit	H_{total} (A/m) rms	% of ICNIRP limit	f_0 (kHz)
ESBs					
E1	10.3	11.8 %	0.015*	< 0.5 %	50
E2	18.1	20.8 %	0.018*	< 0.5 %	47.5
E3	16.1	18.5 %	0.018*	< 0.5 %	47.5
E4	71.6	82.3 %	0.016*	< 0.5 %	47.5
E5	22.2	25.5 %	0.016*	< 0.5 %	37.5
E6	12.9	14.8 %	0.023*	< 0.5 %	40
E7	18.2	20.9 %	0.023*	< 0.5 %	52.5
E8	10.1	11.6 %	0.020*	< 0.5 %	45
E9	12.5	14.4 %	0.031	0.6 %	27.5
E10	10.6	12.1 %	0.018*	< 0.5 %	42.5
E11	17.2	19.7 %	0.029*	0.6 %	42.5
Incandescent Bulbs					
I1	0.2*	< 0.5 %	0.015*	< 0.5 %	*
I2	0.2*	< 0.5 %	0.015*	< 0.5 %	*
LED Bulbs					
L1	0.3*	< 0.5 %	0.016*	< 0.5 %	*
L2	0.6	0.7 %	0.016*	< 0.5 %	65
Noise Floor	0.13		0.015		

* Measurement is below twice the noise level of Narda EHP-200 probe (see Figures 6 and 7). If both E_{total} and H_{total} are below this level, then the operating frequency is not reported.

Table 6: Total electric and magnetic fields directly below the light bulb at a center-to-center distance of 300 mm.

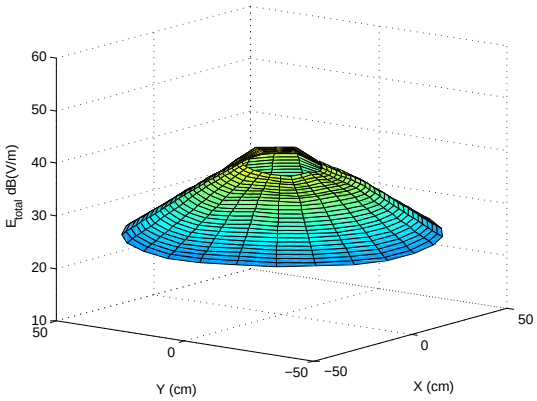

(a) $z = 120\,\mathrm{mm}$

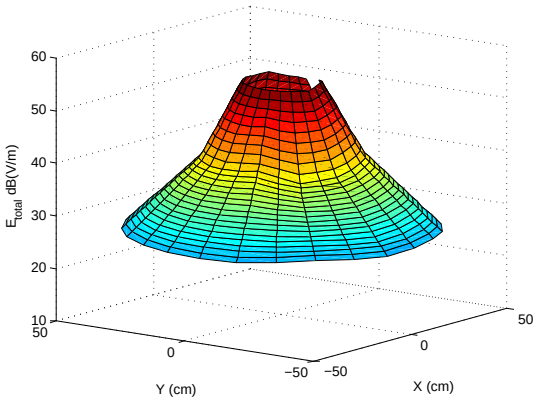

(b) $z = 0\,\mathrm{mm}$

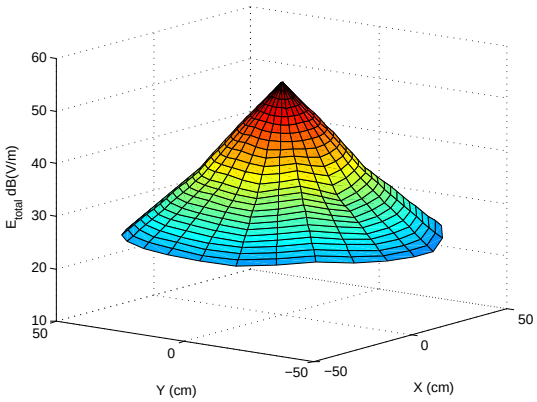

(c) $z = $ -120 mm

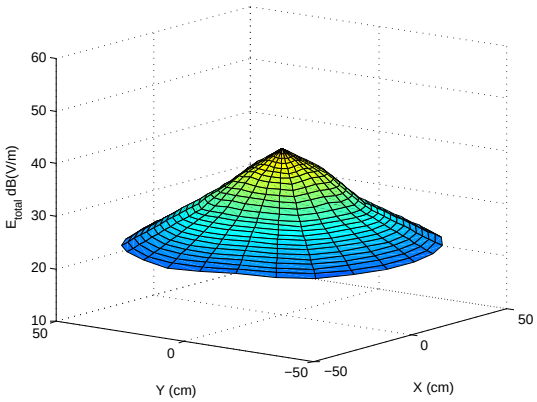

(d) $z = $ -250 mm

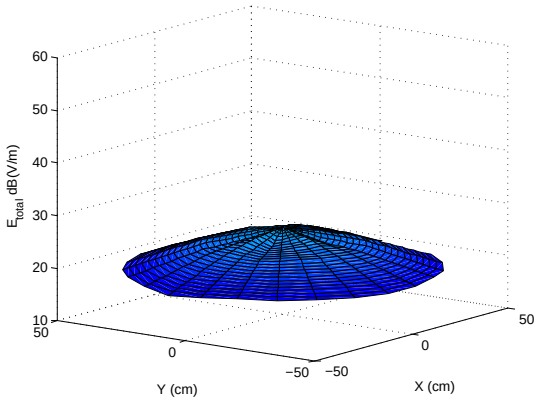

(e) $z = $ -500 mm

Figure 20: Electric field distribution in horizontal slices around the E4 bulb

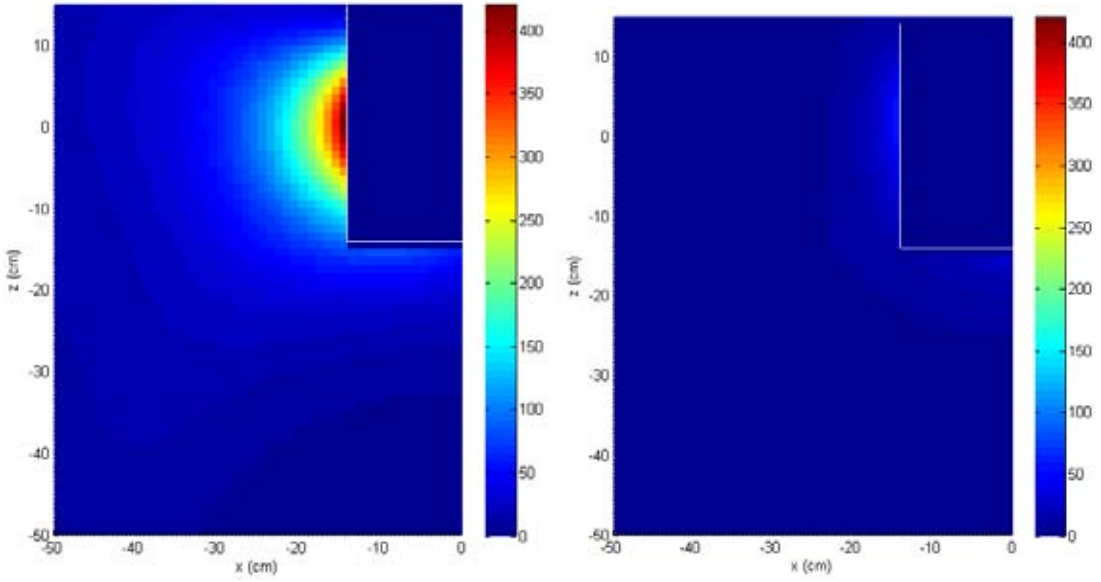

(a) E_x

(b) E_y

(c) E_z

(d) E_{total}

Figure 21: Electric field distributions around the E4 bulb

5.1.1 Fields from Long Fluorescent Tube Lights

Electric and magnetic field components were measured along the length of 1500 mm-long fluorescent tube lights at a distance of 150 mm below the tube light as shown in Figure 22. These tube lights use a passive inductive ballast, rather than an active electronic ballasts like those used for the ESBs. A passive ballast regulates the current but does not transform the 50 Hz signal to a higher frequency signal. Five points were measured at locations which are equally spaced (separation distance of 375 mm) along the length of the tube light with the first and last point being at either ends. Table 7 lists the field intensities and corresponding % of ICNIRP limits. It can be seen that both electric and magnetic fields emanating from the long fluorescent tube lights are close to the noise level. This is due to the use of a passive ballast.

(a) Point 3 (center) (b) Point 4 (c) Point 5 (end)

Figure 22: Locations of measurement points 3, 4, and 5 along the length of fluorescent light at 150 mm directly below it.

Location	E_{total} (V/m) rms	% of ICNIRP limit	H_{total} (A/m) rms	% of ICNIRP limit	f_0 (kHz)
T1					
Point 1	0.71	0.82%	0.015*	< 0.5%	67.5
Point 2	0.80	0.92%	0.015*	< 0.5%	67.5
Point 3	0.89	1.0%	0.015*	< 0.5%	67.5
Point 4	0.87	1.0%	0.015*	< 0.5%	67.5
Point 5	0.69	0.79%	0.015*	< 0.5%	67.5
T2					
Point 1	0.16*	< 0.5%	0.015*	< 0.5%	*
Point 2	0.16*	< 0.5%	0.015*	< 0.5%	*
Point 3	0.16*	< 0.5%	0.015*	< 0.5%	*
Point 4	0.16*	< 0.5%	0.015*	< 0.5%	*
Point 5	0.16*	< 0.5%	0.015*	< 0.5%	*
Noise Floor	0.13		0.015		

* Measurement is below twice the noise level of Narda EHP-200 probe (see Figures 6 and 7). If both E_{total} and H_{total} are below this level, then the operating frequency is not reported.

Table 7: Total electric and magnetic fields measured along the length of the fluorescent tubes at 150 mm directly below them.

5.2 Measurements According to Existing Standard (IEC 62493)

Measurements have been conducted on a select number of light bulbs to assess compliance with the existing IEC standard [1] developed for the evaluation of human exposure to electromagnetic fields from lighting equipment. Figure 23 shows the measurement setup wherein a conducting sphere (in our case, made out of stainless steel) of diameter 210 mm is mounted on an insulating holder 0.86 m above the ground (the standard requires a distance of at least 0.8 m). This sphere, referred to as a "Van Der Hoofden Test-Head", was placed under the ESB at a separation distance of 300 mm as specified in Annex A of the standard. Induced currents on the sphere travel to the protection network by a 0.32 m long wire as shown in the Figure 23 (the standard requires a distance of 0.3 ± 0.03 m). Calibration of the protection network according to Annex F of [1] was confirmed by the supplier of the network. The output of protection network was connected by a coaxial cable to the data acquisition unit placed outside the shielded chamber. The input impedance of data acquisition unit from the specifications is 1 MΩ in parallel with 30 pF. This data acquisition unit connected to a PC via a USB port. It can sample the input voltage at a specified sampling rate. This sampled voltage was recorded and Fast Fourier Transform (FFT) was employed to analyze the spectral content as shown in Figure 24.

Figure 23: Test setup showing protection network connected to the Van Der Hoofden test-head, which was placed under the ESB (E4 bulb) at a separation distance of 300 mm.

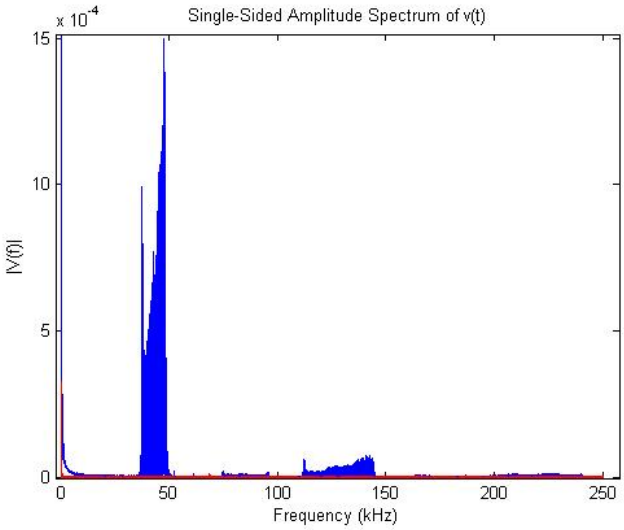

Figure 24: Frequency spectrum of recorded voltage at output of protection network connected to the 'Van Der Hoofden Test-Head' for one ESB (E4 bulb).

$$\sum_{\substack{f_i=20\,kHz \\ step=220\,Hz}}^{150\,kHz} \frac{J_{cap}(f_i,d)}{J_{Lim}(f_i)} + \sum_{\substack{f_i=150\,kHz \\ step=10\,kHz}}^{10\,MHz} \frac{J_{cap}(f_i,d)}{J_{Lim}(f_i)} \leq 0.85$$

where,

$$J_{Lim}(f_i) = \frac{f_i}{500} \cdot 10^{-3} \text{ with } f_i \text{ in Hz} \tag{23}$$

For the first summation, a sampling rate of 500 k samples/sec was used and 65536 samples were recorded resulting in a frequency resolution of 3.815 Hz. For the second summation, a sampling rate of 25 M samples/sec was used and 65536 samples were recorded resulting in a frequency resolution of 190.735 Hz. Since the frequency resolution of the recorded data were different from the step sizes mentioned in equation 23, the recorded data were appropriately power summed to obtain J_{cap} at the required step sizes. The first and second summations for the bulb with highest exposure (E4 bulb) was computed to be 1.6 and 0.12 resulting in a total value of 1.72, which is 201% of the 0.85 limit given in Equation 23. The corresponding percentages for two other bulbs (E3 and E8) were 78% and 24%, respectively. From the extrapolated induced current densities obtained at 20 mm separation distance and conversion factors to anatomical human models given in Table 20 for these three bulbs, the percentages are 55.7%, 17.5% and 11.0% for the E4, E3 and E8 bulbs respectively. Comparing these two methods, the IEC 62493 results are overestimated relative to current density probe measurements. The amount of overestimation varies significantly for these three bulbs. For example, the overestimation for E3 (approximately 4.5) and for E8 (approximately 2.2) are different by a factor of 2 (or 6 dB). This aspect needs to be further investigated.

5.2.1 Drawbacks of IEC 62493 Standard

The following observations have been made about the IEC 62493 standard.

- Since a differential connection to the metallic sphere is not possible, eddy currents induced from incident magnetic fields cannot be measured using the measurement setup of IEC

62493.

- Comparing field levels in Tables 5 and 6, it can be seen that fields decay rapidly with distance in close proximity to the ESBs. Since the metallic sphere is located at a relatively far distance (300 mm), it does not couple with the fields closer to the bulb. This would yield different exposure conditions compared to humans when they are in close proximity to the bulbs.

- The basic restrictions in the ICNIRP guidelines [9] require averaging the currents over a 1 cm^2 cross-sectional area perpendicular to the direction of currents induced inside the body. Polarization of the fields surrounding the ESBs affect the direction of induced currents inside human tissues. Upon using a metallic sphere (isotropic receiver) for measuring incident fields, this information about polarization of incident fields can not be extracted.

- At extremely low frequencies (ELF) and in close proximity to the ESBs, voltages induced from the incident electric fields are a direct result of the capacitance effect between the ESB and the metallic sphere (or human body). Since induced current density is the basic restriction in ICNIRP standard [9], it becomes extremely critical in how this induced voltage is converted into induced currents. The IEC standard uses the transfer function of protection network to convert this voltage into induced currents (J_{cap} in equation 23), which is quite arbitrary, and has no correlation to induced currents in the human body. This means that compliance of lighting equipment based on equation 23, in reality, may or may not imply compliance with the basic restrictions in real human exposure.

5.3 50 Hz Magnetic Field

The incident magnetic field at 50 Hz from the bulbs was measured using the Narda ELT-400 probe (Figure 8) at a distance of 150 mm (center of bulb to center of probe). 50 Hz B-field was measured at two locations: below the bulb and to the side of the bulb as shown in Figure 25. At these locations, ELT-400 probe was rotated in all angles both in azimuth and elevation planes to capture the peak rms field. Narda ELT-400 probe was set to the range 30 Hz — 400 kHz and the rms reading from the probe was manually recorded. Since the magnetic field components emanating from the bulb for frequencies above 9 kHz are negligible (as seen on EHP-200 probe), this measured field value is predominantly going to be at 50 Hz considering that the bulb's fundamental frequencies are in the range of 30 — 50 kHz.

Table 8 lists the recorded rms B-field at both locations and their corresponding percentage of the ICNIRP limit. In addition to the bulbs, 50 Hz magnetic field was measured for a 100 W rated 4.1 kΩ resistor which was connected to the bulb holder as shown in Figure 26. A 4.1 kΩ resistor was chosen because it dissipates 12.8 W of power (similar to most compact ESBs chosen for this study) from the 230 V mains. Furthermore, this resisitor load was connected to the bulb holder such that it occupies a similar physical size (separating +ve and -ve of mains) as that of a compact ESB. It can be seen from Table 8 that the B-field emanating from the resistor load is of the same order of magnitude as that from all the compact ESBs. This demonstrates that the ESB doesn't generate a significant 50 Hz B-field beyond what is generated from a current flowing in a loop of a similar size.

The higher 50 Hz B-field field from the fluorescent tube lights is apparent, given that the passive inductive ballast that is used generates a significant magnetic field. Also, the generation of a 50 Hz B-field depends on the physical size of the load and the amount of current it draws from the mains (power consumption). In addition to measuring the 50 Hz B-field under the center of the long fluorescent tube light, the probe was swept along the length to find the maximum B-field location. The B-field was recorded at this location, which was approximately

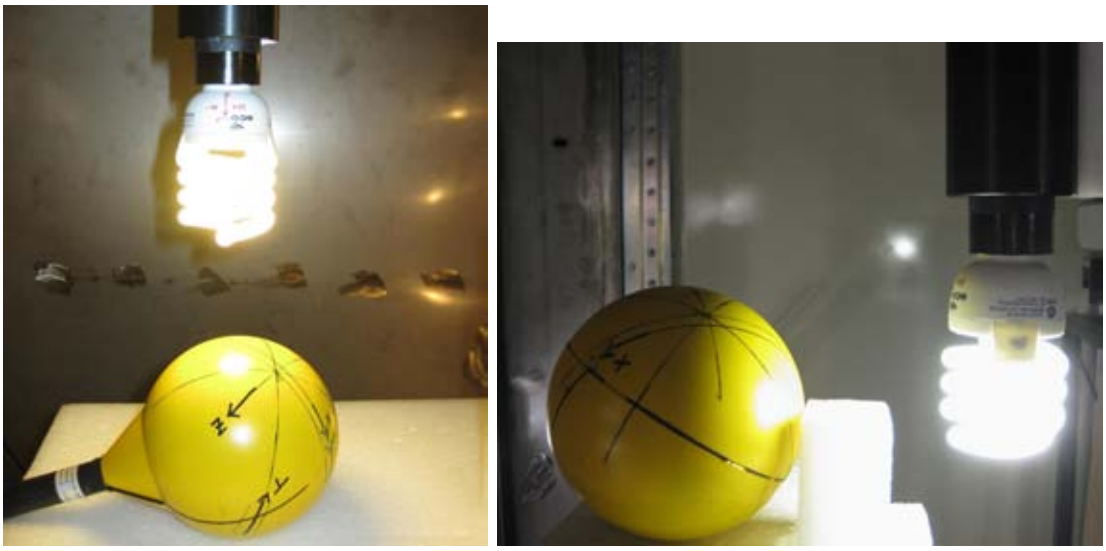

(a) 150 mm below the bulb (b) 150 mm to the side of the bulb

Figure 25: Locations of 50 Hz B-field measurements using the Narda ELT-400 probe.

under the inductive ballast box present inside the shielded holder for both the tube lights. Both these values were recorded as shown in the Table 8.

Due to the relatively high B field measured directly under the fluorescent tube lights, the two-dimensional distribution of the B field has been measured under one of them (T1). The results are shown in Table 9. The measured points along the length of the fluorescent tube light are the same as those described in Figure 22. The peak value in Table 9 is less than the peak value of Table 8 because the two-dimensional distribution was scanned at fixed points which do not include the location of the peak B-field. Table 9 can be used to determine the distance from the tube at which the B-field is below a certain value.

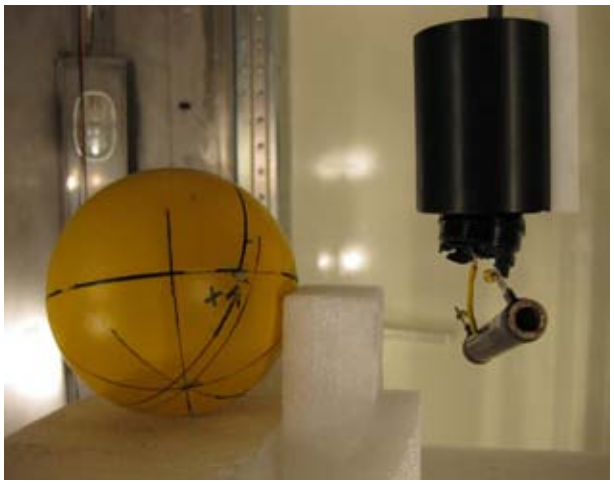

Figure 26: 50 Hz B-field measurement of 4.1 kΩ resistor load drawing 12.8 W of power.

Bulb	B_{total} (nT) rms 150 mm below the bulb	% of ICNIRP (100 μ T)	B_{total} (nT) rms 150 mm to side of the bulb	% of ICNIRP (100 μ T)
ESBs				
E1	52	$< 0.5\%$	61	$< 0.5\%$
E2	58	$< 0.5\%$	70	$< 0.5\%$
E3	103	$< 0.5\%$	99	$< 0.5\%$
E4	173	$< 0.5\%$	193	$< 0.5\%$
E5	282	$< 0.5\%$	382	$< 0.5\%$
E6	212	$< 0.5\%$	183	$< 0.5\%$
E7	198	$< 0.5\%$	227	$< 0.5\%$
E8	60	$< 0.5\%$	56	$< 0.5\%$
E9	191	$< 0.5\%$	340	$< 0.5\%$
E10	72	$< 0.5\%$	67	$< 0.5\%$
E11	301	$< 0.5\%$	362	$< 0.5\%$
Incandescent Bulbs				
I1	70	$< 0.5\%$	81	$< 0.5\%$
I2	48	$< 0.5\%$	47	$< 0.5\%$
LED Bulbs				
L1	61	$< 0.5\%$	61	$< 0.5\%$
L2	143	$< 0.5\%$	109	$< 0.5\%$
Long Fluorescent Tube Lights				
T1	1057	1.1% (center)		
	4115	4.1% (max)		
T2	1075	1.1% (center)		
	4186	4.2% (max)		
Noise Floor	48			
4.1 kΩ Resistor	161	$< 0.5\%$	95	$< 0.5\%$

Table 8: 50 Hz B-field measurements 150 mm below and to the side of the bulb.

	Location Along Tube				
z (mm)	Point 1	Point 2	Point 3	Point 4	Point 5
150	248	2651	967	254	133
300	122	714	358	93	51
500	74	174	146	59	44
1000	42	48	47	48	48

Table 9: Two-dimensional distribution of 50 Hz B-field measurements under the Micasa MI-GROS Combilux tube.

6 WP4 - Assessment of the Induced Fields

6.1 Procedure for Computing the Current Density

The frequency spectrum of the measured current density is shown in Figure 27 for two bulbs: the E4 bulb (ESB) and the L2 bulb (LED bulb). The ESB has a significant signal at frequencies near 40 kHz and at odd harmonics of this frequency. On the contrary, the LED bulb does not emit significant signal above the noise floor in this frequency range. ICNIRP has published guidelines to compute net current density for non-sinusoidal signals having a wide-range of frequency components which are non-coherent in nature [9]. As can be seen from the frequency spectrum in Figure 27, it has a relatively wide-band (about 10 kHz) and contains significant power at higher harmonics. For such a signal occupying large band of frequencies, it is not straighforward to check its compliance with ICNIRP limits which are frequency dependant. This section describes the procedure used to evaluate compliance following the guidelines given in [9].

The voltage across the current clamp was captured over time with a sampling rate much higher than the frequencies of interest (in this case, 2 M samples/sec covering frequencies with Nyquist limit of 1 MHz) as shown in Figure 28. This time-domain voltage signal was decomposed into its spectral components by applying a Fast Fourier Transform (FFT) depending on the number of time samples captured (see Figure 29). Dividing this value by the transfer impedance of the current clamp (see Figure 15) results in a frequency spectrum of induced current. Further dividing this with the cross-sectional area of the saline phantom results in a spectral content of the induced current density. Since the current clamp was designed for frequencies greater than 20 kHz, this frequecy spectrum was high pass filtered with a cutoff frequency at 20 kHz. Such high pass filtering is quite reasonable considering that most lighting equipment does not have frequency content below 20 kHz. Manufacturers design them in order to avoid audible noise and interference to household electronics in the audio band. In addition to high pass filtering, the presence of a noise source at 350 kHz was suppressed using a notch (narrow band-stop) filter around that frequency. Care was taken to make sure spurious frequencies resulting from sampling and windowing (while computing the FFT) were also filtered out.

Since the ICNIRP limits are frequency dependent in this frequency range ($f/500\,\mathrm{mA/m^2}$), the frequency spectrum of the induced current density was weighted with a filter function centered around the peak frequency f_0 (e.g., $f_0 = 47\,\mathrm{kHz}$). Frequencies below f_0 were amplified and frequencies above f_0 were attenuated proportional to (f_0/f). The inverse FFT was applied on the resulting frequency-compensated spectrum to obtain the time-domain signal of induced current density as shown in Figure 30. The rms value was computed over the entire time-captured signal and this was compared with the ICNIRP limit at the peak frequency ($f_0/500$) to obtain the percent of the ICNIRP limit.

Variations in the peak amplitude of the time-captured data (see Figure 28) from the current clamp exist due to the electronic ballast circuitry. Due to the limitations of the data acquisition unit, we cannot capture many such peaks over a long duration of time with such a high sampling rate (2 M samples/sec). Therefore, we analyzed the uncertainty due to the sampling duration. The bulb with the largest amplitude variation (E4 bulb) was monitored over 15 minutes by capturing 32 ms of time-domain voltage (approximately the maximum amount of data-capture at this sampling rate) at the current clamp at regular intervals (every 15 seconds). The induced current density was computed for each 32 ms sample. The results are shown in Figure 31. Note that the bulb was turned on for at least 10 minutes before these starting these measurements. The standard deviation was found to be 3.5% of the average. This value was accounted for in the uncertainty budget for induced current density measurements (see Table 23).

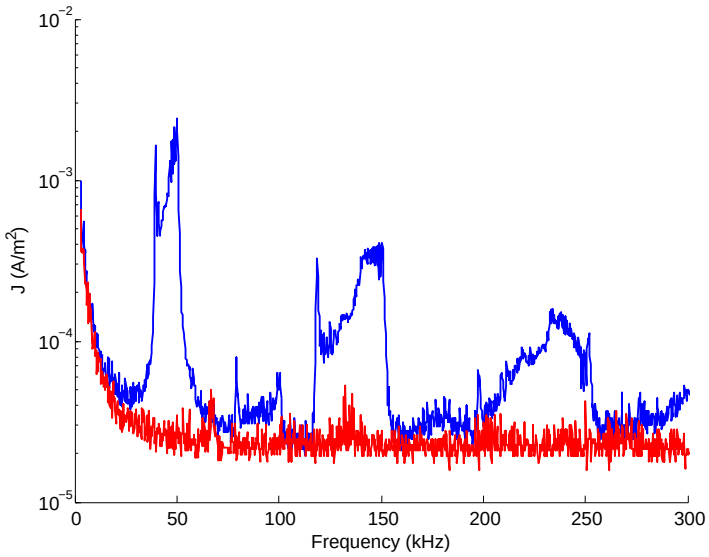

Figure 27: Frequency spectrum of the current density for one ESB (blue line, E4 bulb) and one LED bulb (red line, L2 bulb).

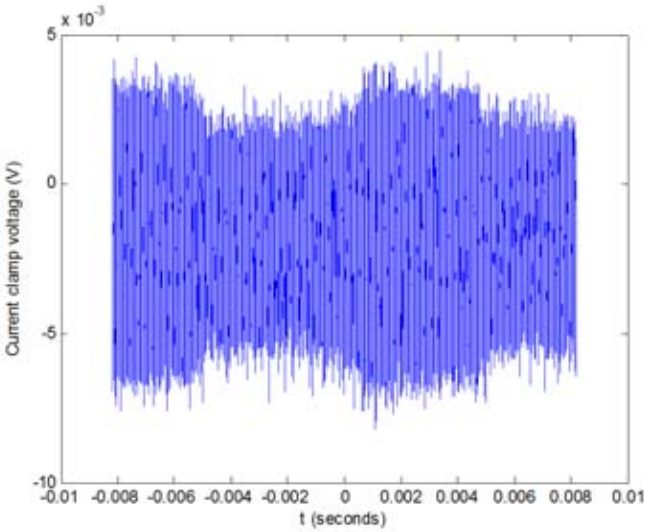

Figure 28: Time-captured voltage signal of current clamp for a ESB (E8 bulb) at a separation distance of 20 mm.

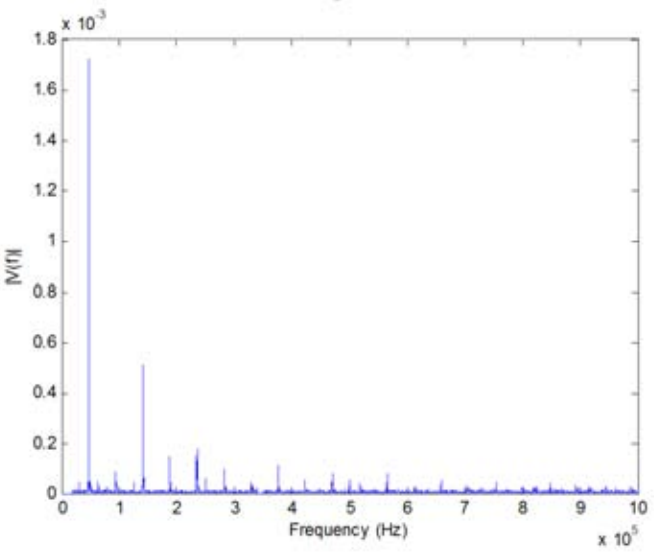

Figure 29: Spectral content of current clamp's time-captured voltage signal for a ESB (E8 bulb) at a separation distance of 20 mm.

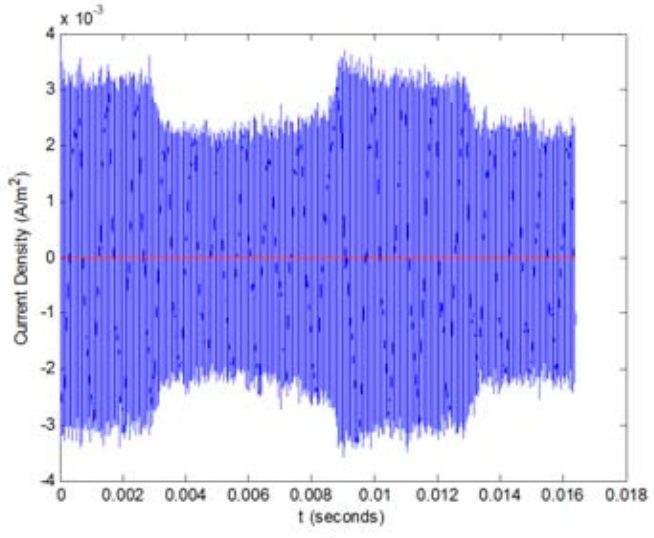

Figure 30: Post-processed induced current density signal vs. time for a ESB (E8 bulb) at a separation distance of 20 mm.

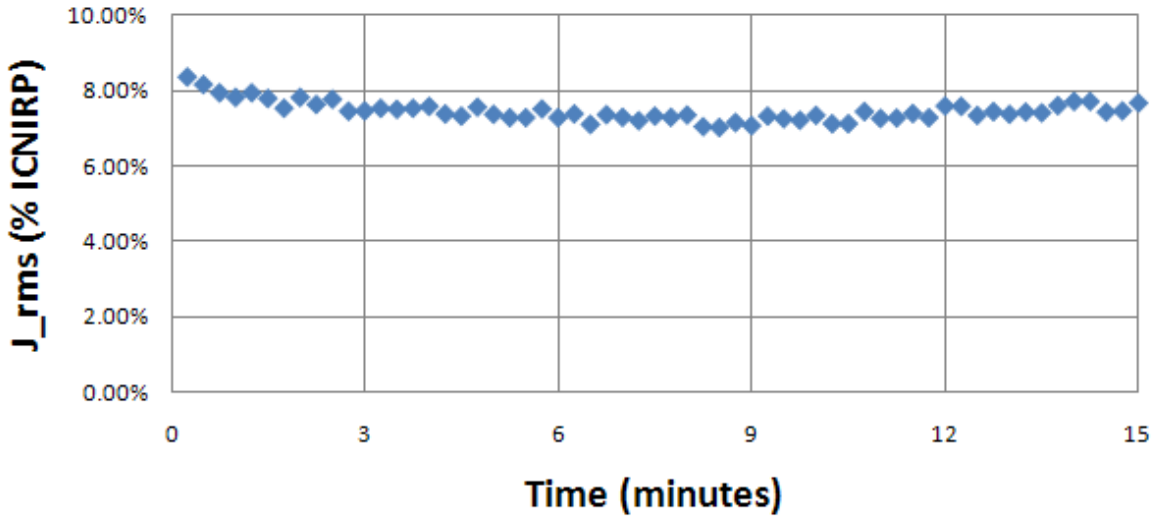

Figure 31: Variation in % of ICNIRP limit (from rms of induced current density time-signal over short durations) for E4 bulb over 15 minutes at a separation distance of 20 mm.

6.2 Measurements

The induced current densities for all bulbs under investigation were measured at two separation distances: 20 mm below the bulb (Table 10) and 50 mm to the side of the bulb (Table 11). Components J_x and J_z are shown; J_y is not shown, as it was found to be negligible. For the 20 mm distance below the bulb, the J_z component is measured with the current density probe oriented as shown in Figure 3 (also similarly to Figure 35), while the J_x component is measured with the current density probe oriented horizontally and the center of the current clamp directly under the center of the bulb (similarly to Figure 34). For the 50 mm distance to the side of the bulb, the J_z component is measured with the current density probe oriented vertically and the center of the current clamp directly to one side of the center of the fluorescent tube, while the J_x component is measured with the current density probe oriented horizontally and the center axis of the probe at the center of the fluorescent tube. The larger distance for measurements made at the side of the current density probe is due to the styrofoam support for the current density probe, which restricts how close the probe can get when measuring on the side. For the measurements to the side of the bulb, each bulb was rotated about its vertical axis and the maximum current density was recorded.

	J_x ($\mathrm{mA/m^2}$) rms	J_z ($\mathrm{mA/m^2}$) rms	% of ICNIRP limit	f_0 (kHz)	Output Power (W)
ESBs					
E1	0.17*	1.70	1.8%	46.5	8
E2	0.34*	2.40	2.8%	43.6	18
E3	0.19*	2.20	2.9%	37.7	12
E4	0.43*	8.60	9.1%	47.1	20
E5	0.47*	2.20	3.0%	36.9	20
E6	0.26*	1.40	1.9%	37.7	11
E7	0.18*	3.50	3.6%	48.8	20
E8	0.33*	1.70	1.8%	47.1	11
E9	0.12*	0.84	1.6%	26.2	11
E10	0.26*	1.20	1.4%	41.5	12
E11	0.27*	2.50	3.1%	40.2	20
Incandescent Bulbs					
I1	0.36*	0.23*	$< 0.5\%$	*	75
I2	0.25*	0.24*	$< 0.5\%$	*	60
LED Bulbs					
L1	0.31*	0.51*	$< 0.5\%$	*	8
L2	0.30*	0.51*	$< 0.5\%$	*	1.5
Noise Floor	0.29	0.29	N/A	N/A	N/A

* Measurement of J_x or J_z is below a value of twice the noise floor. If one value is below this value, the percentage of the ICNIRP limit is calculated from the other value alone. If both J_x and J_z are below this value, the peak frequency is not reported, and the percentage of the ICNIRP limit is stated as being less than 0.5%.

Table 10: Induced current density in the horizontal (x) and vertical (z) polarizations of the current density probe measured below the light bulb with a separation distance of $d_J = 20$ mm.

As expected, the fields are radiating radially outward from the bulb with a vertical component (J_z) dominant when measured under the bulb and horizontal component (J_x) when measured

	J_x (mA/m^2) rms	J_z (mA/m^2) rms	% of ICNIRP limit	f_0 (kHz)	Output Power (W)
ESBs					
E1	1.54	0.55*	1.7%	46.5	8
E2	2.23	1.03	2.8%	43.6	18
E3	1.91	0.73	2.7%	37.7	12
E4	7.17	1.82	7.9%	47.1	20
E5	2.46	0.78	3.5%	36.9	20
E6	1.68	1.09	2.7%	37.7	11
E7	3.16	0.64	3.3%	48.8	20
E8	1.69	0.63	1.9%	47.1	11
E9	0.92	0.27*	1.8%	26.2	11
E10	1.15	0.44*	1.4%	41.5	12
E11	3.24	0.92	4.2%	40.2	20
Incandescent Bulbs					
I1	0.33*	0.71	0.5%	68.0	75
I2	0.26*	0.42*	$< 0.5\%$	*	60
LED Bulbs					
L1	0.51*	0.34*	$< 0.5\%$	*	8
L2	0.47*	0.33*	$< 0.5\%$	*	1.5
Noise Floor	0.29	0.29	N/A	N/A	N/A

* Measurement of J_x or J_z is below a value of twice the noise floor. If one value is below this value, the percentage of the ICNIRP limit is calculated from the other value alone. If both J_x and J_z are below this value, the peak frequency is not reported, and the percentage of the ICNIRP limit is stated as being less than 0.5%.

Table 11: Induced current density in the horizontal (x) and vertical (z) polarizations of the current density probe measured to the side of light bulb with a separation distance of $d_J = 50\,\text{mm}$.

to the side of the bulb. Similar to the incident electric fields, induced current densities are higher for the ESBs than for the incandescent and LED bulbs. The current densities for the incandescent bulbs are negligible, as the measured values are in the noise levels of the equipment.

For the ESBs studied, the ICNIRP-normalized current densities vary by a factor of more than six. As expected, there is a general trend between induced current density and the output power for the ESBs, with the highest power-rated bulbs having the highest current densities, as shown in Figure 32. However, the exposure still varies by a factor of almost four for bulbs having the same output power. It should be noted that this variation is largely due to E3 and E4 models, which are not available in Switzerland at this time. If these two bulbs are removed from consideration, the current density of the remaining bulbs varies by a factor of two after normalizing the bulbs for the stated output power.

Ten bulbs of the same manuafacturer and model (E2 bulb) were also measured to check manufacturing variation, as shown in Table 12. The results show that the standard deviation of the measured current density is within the measurement uncertainty. This is not a large statistical sample and it is only of one make and model of ESB. Therefore, the authors do not claim that this data represent a typical manufacturing variation of ESBs.

Bulb	J_z (mA/m^2) rms	f_0 (kHz)
1	2.92	43.5
2	2.32	42.1
3	2.12	42.3
4	2.53	44.9
5	2.57	43.3
6	2.25	43.2
7	2.09	43.3
8	2.59	44.3
9	2.45	43.5
10	2.16	43.9
Standard deviation (mA/m^2)	0.26	
Standard deviation (%)	11%	

Table 12: Variation in the induced current density for 10 light bulbs of the same make and manufacturer (E2). Measurements were made for the vertical (z) polarization of the current density probe when measured below the light bulb with a separation distance of $d_J = 20\,\text{mm}$.

Figure 33 shows the measured current density J_z as a function of distance d_J when the current density probe is located directly under the bulb, as shown in Figure 3. This figure shows that the current density drops exponentially with distance to the light source.

6.2.1 Effect of the Height over the Ground Plane

Induced current density measurements so far were performed with the bulb hanging in the middle of the shielded chamber at a height of 1200 mm above the ground. Induced current density measurements were performed on the bulb with the highest exposure (E4 bulb) at different heights (every 150 mm) of the bulb over the ground plane to assess the effect of height. Table 13 shows the induced current density values at different heights measured with current density probe placed under the bulb at a constant separation distance of $d_J = 20\,\text{mm}$. At the bulb's lowest height of 500 mm over ground plane, the current density probe (having a length of 420 mm plus the reinforcing foam block surrounding it - see Figure 3) placed under the bulb

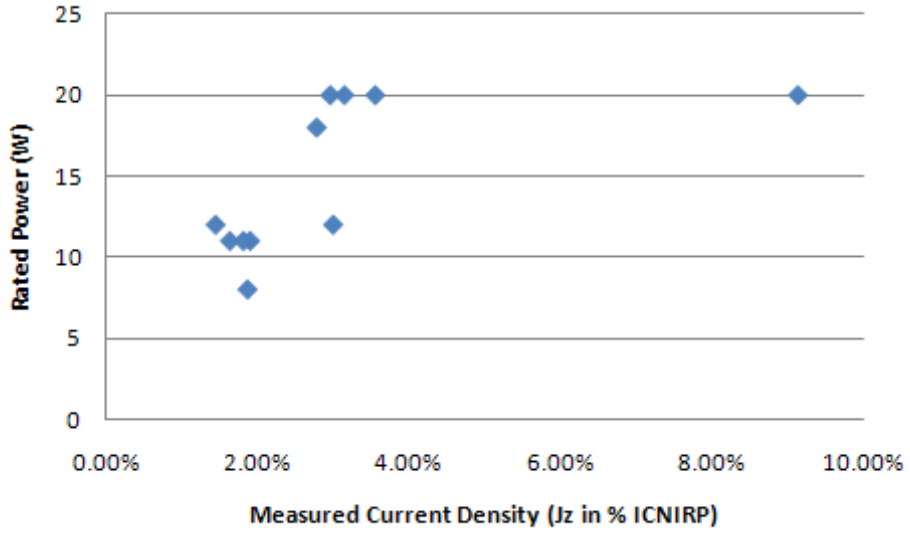

Figure 32: Current density J_z vs output power for the eleven ESBs investigated at a separation distance of 20 mm.

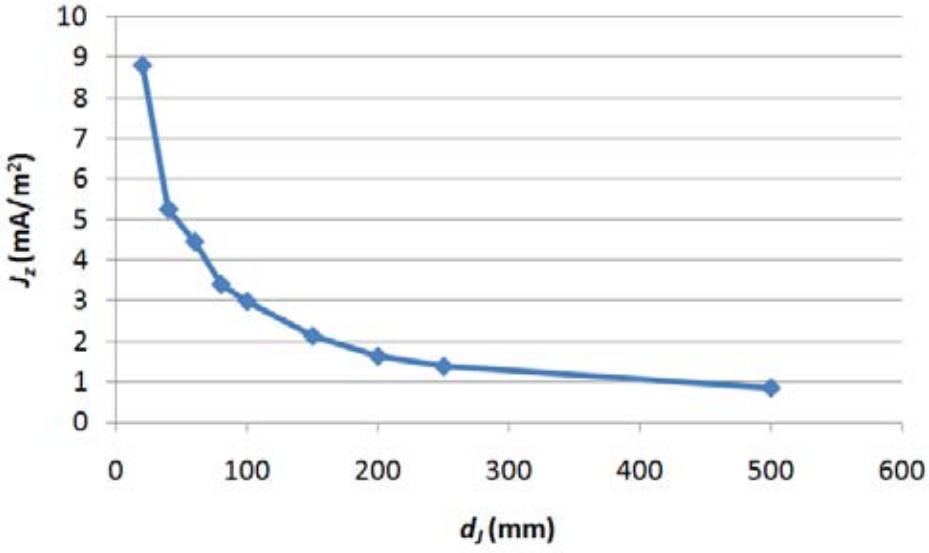

Figure 33: Current density J_z versus distance d_J for exposure directly under the E4 bulb.

was almost resting on the ground plane. From the table, it can be seen that height above the ground plane did not significantly alter the results. However, this parameter (height of bulb above the ground plane) needs to be standardized and environment where the measurements were conducted should be specified. This requires further investigation. Also note that the grounded metallic floor is an extreme case for assessing the effect of height over ground plane when compared to a non-conducting floor.

Height of bulb above GND plane (mm)	J_z (mA/m^2) rms	% of ICNIRP limit
500	8.47	8.9%
650	7.71	8.1%
800	8.19	8.6%
950	6.32	6.7%
1100	7.43	7.8%
1250	8.42	8.9%

Table 13: Induced current density at 47.5 kHz in vertical polarization of the current density probe measured under E4 bulb with a constant separation distance of 20 mm at varying heights of bulb over the ground plane.

6.2.2 Induced Currents from Long Fluorescent Tube Lights

Similar to electric and magnetic field measurements, induced current densities in both horizontal and vertical polarizations using the current density probe were measured along the length of the 1500 mm-long fluorescent tube lights. Five points were measured at locations which are equally spaced (separation distance of 375 mm) along the length of the tube light with the first and last point being at either ends. The horizontal polarization was measured at a separation distance of 50 mm between the tube light and the side of the current density probe (see Figure 34) whereas, the vertical polarization is measured with a separation distance of 20 mm (see Figure 35). The different distances for the two phantom orientations are due to the fact that the probe support does not allow 20 mm separation distance in the horizontal orientation. Table 14 lists the induced current densities and their corresponding % of ICNIRP limits for both polarizations. It can be seen that similar to electric and magnetic fields, induced currents in the current density probe from the long fluorescent tube lights are close to the noise levels, due to the passive ballast that is used.

(a) Point 3 (center) (b) Point 4 (c) Point 5 (end)

Figure 34: Horizontal polarization (J_x) of the current density probe measured at points 3, 4, and 5 along the length of fluorescent tube light with a vertical separation distance of 50 mm between the closest points of the fluorescent tube and the current density probe.

(a) Point 3 (center) (b) Point 4 (c) Point 5 (end)

Figure 35: Vertical polarization (J_z) of the current density probe measured at points 3, 4, and 5 along the length of fluorescent tube light with a vertical separation distance of 20 mm between the closest points of the fluorescent tube and the current density probe.

Location	J_x (mA/m^2) rms	J_z (mA/m^2) rms
T1		
Point 1	0.26*	0.23*
Point 2	0.28*	0.37*
Point 3	0.49*	0.37*
Point 4	0.35*	0.27*
Point 5	0.51*	0.26*
T2		
Point 1	0.16*	0.15*
Point 2	0.15*	0.19*
Point 3	0.15*	0.19*
Point 4	0.18*	0.21*
Point 5	0.28*	0.21*
Noise Floor	0.27	0.32

* Measurement is below twice the noise floor of current density equipment (see Figure 18)

Table 14: Induced current density in horizontal and vertical polarizations of current density probe measured along the length of the fluorescent tube light with a separation distance of 50 mm and 20 mm respectively.

6.3 Relationship Between Phantom and Human Models

In this section, a conservative relationship is developed between the current densities measured in the current density probe and the current densities found in anatomical human models. For two exposure scenarios, the current density probe and the four anatomical human models of Section 4.5.2 were simulated using SEMCAD X, as described in Section 4.5.1. The first exposure scenario provides a relatively uniform exposure and the second scenario provides a non-uniform source exposure. Current density results are averaged over an area of 1 cm^2 perpendicular to the direction of current flow at all locations in the body, as specified by ICNIRP [9]. The peak value obtained after averaging is reported. All these simulations were performed at 100 kHz unless otherwise specified. These are described in the following subsections.

6.3.1 Uniform Exposure

For the first exposure scenario, a parallel plate capacitor has been modeled, as shown in Figure 36. Anatomical human models and the current density probe model were placed in vertical orientation (z) at the geometric center of the parallel plate capacitor. The axis between the plates is also vertically oriented so as to align with the length of human models and current density probe. It has been verified that the current density for the vertical orientation of the plates gives the highest exposure compared to the x and y horizontal plate orientations (by a factor of at least 2.5). The voltage excited across the gap between the plates has been set so that the electric field at the center of the capacitor is 100 V/m when no body or phantom models are present. The size of the capacitor has been chosen to maintain a uniform distribution of the electric field within ± 0.5 dB in the volume occupied by the body model when the capacitor is empty. A cubical volume with dimensions of twice the height of the human model achieves this uniformity. For example, for the Duke model, the size of the plates is 3.6 m x 3.6 m, and the separation distance between the plates is 3.6 m.

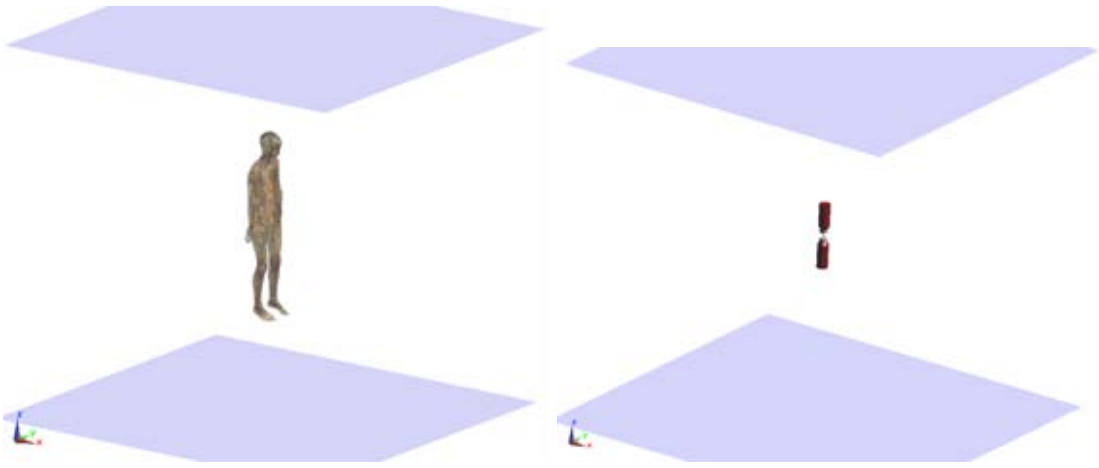

(a) Billie (b) Current density probe

Figure 36: Setup of the Billie model and current density probe in the parallel plate capacitor.

The results are shown in Table 15 for the four cases. The peak current density is in the Achilles tendons, with relatively high values also in the knees. This is expected, as these are narrow pathways for current to flow, resulting in higher current density. The current density in the head is more than 10 dB below the peak current densities.

The current density for the current density probe is nearly identical for all four sizes of the parallel plate capacitor. This verifies that the results are correctly normalized to the same source

conditions for the four cases. It is seen that the highest current density occurs for the Duke model, although the results are not strongly dependent on the body model. The highest average current density for this model is 6.7 times higher than that for the current density probe.

Name	J (mA/m^2) human	J (mA/m^2) probe	Ratio
Duke	223	33.5	6.7
Ella	178	33.5	5.3
Billie	198	33.0	6.0
Thelonious	159	34.0	4.7

Table 15: Calculated current densities for the four anatomical models and the current density probe.

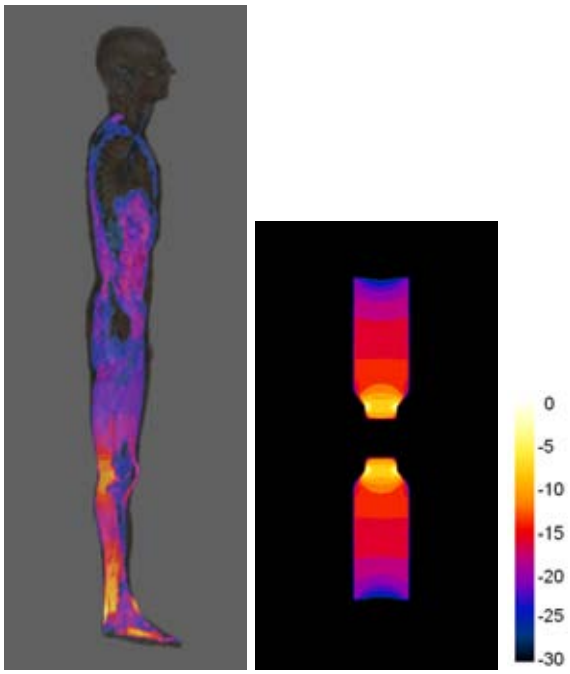

(a) (b)

Figure 37: Current density from the parallel plate capacitor setup in the (a) Duke model and (b) current density probe.

6.3.2 Non-Uniform Exposure

A second exposure scenario has also been investigated, as shown in Figure 38. This exposure scenario is meant to approximately replicate the case of a person standing directly under a light bulb while being grounded at the feet. The Duke model and the current density probe are exposed to a field from a small charged sphere located directly above them. The diameter of the sphere is 50 mm. The charged sphere is at an electric potential of 200 V for all simulations. The Duke model is contacting the ground plane. Due to the slight downward angle of the feet of the Duke model, metal wedges were added to ensure that contact is made with the ground plane along the length of the feet. Three values were chosen for the distance of the metal sphere to the

Duke model or current density probe. The distances from the bottom of the metal sphere to the top of the head or the top of the current density probe are $d_J = 20\,\text{mm}$, 65 mm and 265 mm. First separation distance corresponds to most of the current density probe measurements performed in this study.

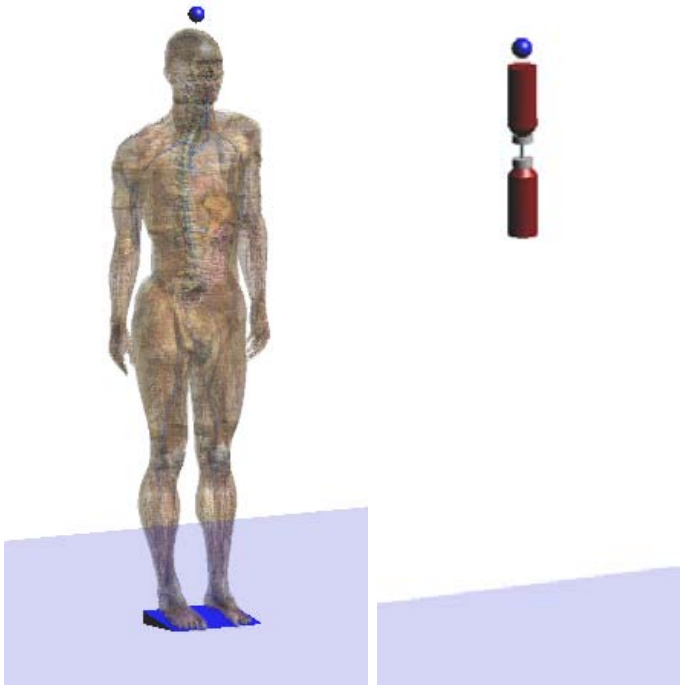

(a) Duke (b) Current density probe

Figure 38: Setup of the exposure to a small charged sphere for the (a) Duke and (b) current density probe.

The results are shown in Table 16 and in Figure 39. The peak current density for the Duke model is in the Achilles tendon, just as it is for the parallel plate capacitor exposure. However, there are also relatively high exposures in the brain region for this case (within 3 dB for the 1 cm^2 average). The same result was observed for the Billie model for the uniform exposure case (not shown): the highest averaged value was found near the ankle, but high values in the brain and spine were also observed. The location of the peak exposure can be sensitive to the type of averaging applied (e.g., averaging over a cross section of the same type of tissue would provide different results). It is therefore recommended that ICNIRP considers this issue and provides clarification on the current density averaging.

d_J (mm)	J (mA/m^2) Duke	J (mA/m^2) Probe	Ratio
20	137	29.3	4.7
65	91.9	18.2	5.0
265	47.3	7.9	6.0

Table 16: Current densities in the Duke model and the current density probe from the charged sphere at three distances.

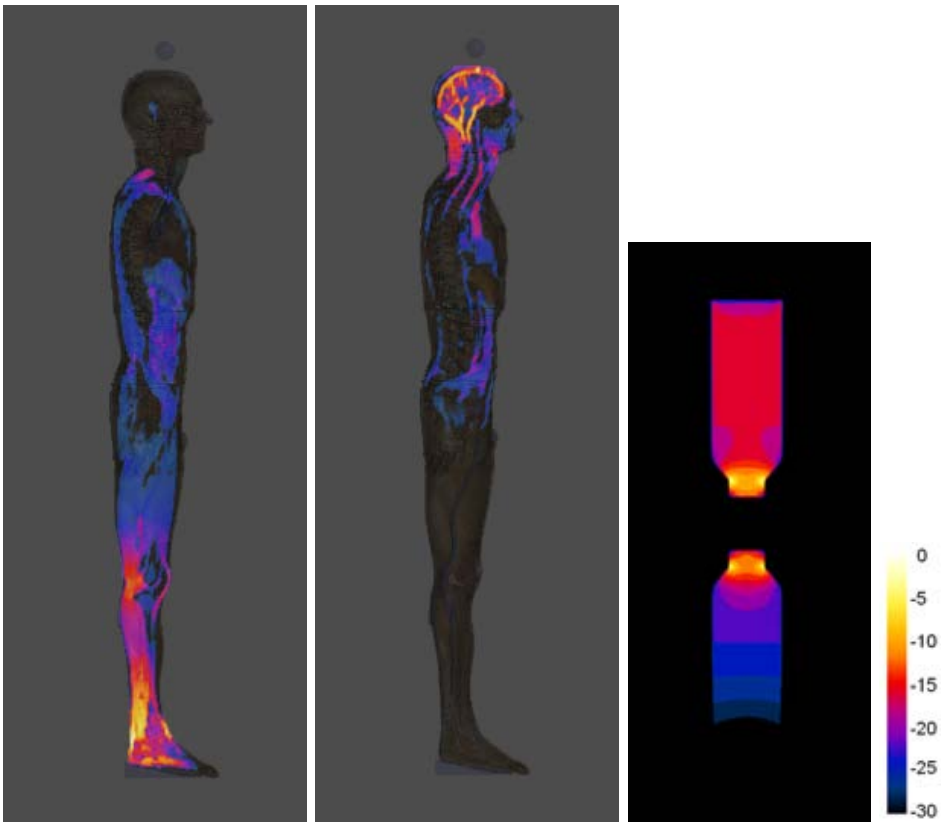

(a) Duke, ankle currents (b) Duke, head currents (c) Current density probe

Figure 39: Current density distributions in two different vertical slices of Duke model (a) and (b), and one vertical slice through the center of the current density probe (c) exposed to a small charged sphere.

The highest average current density for this model is 6.0 times higher than that for the current density probe. The ratios of current densities between the Duke model and the current density probe are quite consistent for the three distances selected. These ratios are also similar to the ratios found for the parallel plate capacitor exposure.

6.3.3 Non-Uniform Exposure: Child Models

Child models (Billie and Thelonious) were also assessed for non-uniform exposure to see if conversion ratios in these models are any different than those reported for Duke model in Table 16. Billie (11-year old) and Thelonious (6-year old) models were placed under a charged sphere separated by $d_J = 20\,\text{mm}$, 65 mm and 265 mm with their feet grounded using metallic wedges to get a better contact with the ground plane. Similar conditions were simulated with current density probe placed under charged sphere and ground plane located at the same distance from charged sphere as in Billie and Thelonious models. Table 17 shows the ratios for Billie and Thelonious models.

Nearest distance (mm)	J (mA/m^2) Human	J (mA/m^2) Probe	Ratio
Billie			
65	110	18.1	6.1
265	52.9	7.8	6.8
Thelonious			
20	196	29.2	6.7
65	119	18.0	6.6
265	54.9	7.6	7.2

Table 17: Current densities in the Billie and Thelonious models and the current density probe from the charged sphere at three distances.

6.3.4 Non-Uniform Exposure: Effect of Ground Plane

So far, all simulations for non-uniform exposure were performed with the feet of human models contacting the ground plane (using metallic wedges under the feet for better contact) in order to induce higher currents. In order to verify that the presence of a ground plane results in higher induced currents, one more scenario is simulated with the Duke model floating in free space without ground plane. This resulted in lowering the 1 cm^2 averaged induced current density from 137 mA/m^2 to 80.1 mA/m^2 when Duke model was exposed to charged sphere separated by a distance of 20 mm. This was expected since the presence of a ground plane (zero potential) intensifies the vertical component of the E-field. This in turn would drive strong induced currents in the body (located in between the charged sphere and ground plane). Also note that, in the absence of ground plane, the location of peak current density changed from Achilles tendon to brain region.

6.3.5 Non-Uniform Exposure: Effect of Location of Charged Sphere Near Body

Two other cases were simulated with the charged sphere (approximately representing an ESB) close to different locations on the body to verify if the location above the head gives the highest exposure for the same separation distance. As seen in Figure 40, the charged sphere was placed close to the chest and stomach of the Duke model. These locations are quite arbitrary but the intent was to assess the induced currents when a person is standing next to a reading lamp or a bed-side lamp. In all these simulations, the charged sphere was located at a separation distance of 20 mm to the nearest part of the body and ground plane was removed. The ground plane was avoided for this comparison because its presence would alter the exposure conditions because E-field intensity incident on the body would be different for varying heights of charged sphere above the ground plane. Table 18 shows the resulting 1 cm^2 averaged induced current density

for various locations of charged sphere. The highest currents were induced in the body when the charged sphere was located above the head. This can be explained due to the fact that the exposure from charged sphere is radially outward and maximum currents will be induced when the length of the body is aligned axially to the source. When the charged sphere was located near chest and stomach, length of the body was only partially aligned compared to the case when the body was directly below the charged sphere. For the same reason, charged sphere located near the stomach would result in inducing minimal currents because the length (larger dimension) of the body is orthogonal to the radial fields emanating from the bulb.

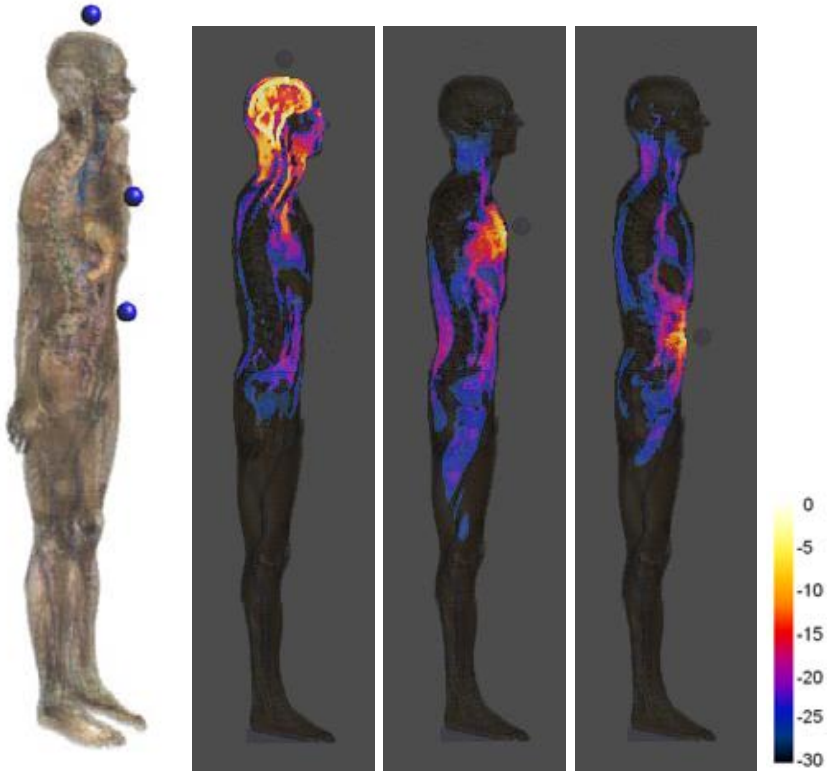

(a) (b) (c) (d)

Figure 40: Current density in the Duke model exposed to a charged sphere at three locations on the body. (a) Locations of the charged sphere; Induced currents in a vertical plane containing the peak value for the three locations of (b) head, (c) chest and (d) stomach.

Location of charged sphere	Nearest distance (mm)	J (mA/m^2)
Head	20	80.1
Chest	20	43.2
Stomach	20	36.4

Table 18: Current densities in the Duke model with the charged sphere at three different locations (head, chest and stomach) in the absence of ground plane.

6.3.6 Non-Uniform Exposure: Effect of Different Postures of Body

In order to identify the worst-case exposure, different postures of the body were simulated to see how it affects induced current density. POSER feature in SEMCAD X was used to orient the Duke model in two different postures as shown in Figure 41. The first posture shows the Duke model with its right arm raised reaching for the bulb. This posture was chosen to replicate a person who is trying to reach for the bulb (hanging from the ceiling or mounted on a reading/table lamp). Second posture shows the Duke model in a sitting position with the bulb located above the head. Both these postures were simulated with the feet of Duke model grounded and with the charged sphere located above the head at separation distances of d_J = 20 mm, 65 mm and 265 mm. Table 19 shows the induced current densities and corresponding ratios obtained when compared to induced currents in current density probe under similar conditions. In the arm raised posture, peak currents were induced in fingers and wrist whereas, in the sitting posture, peak currents were in Achilles tendon. The first posture with the arm raised resulted in the highest observed conversion factor of 10.2 (for simulations conducted at 100 kHz). This is due to the small cross-section of fingers and wrist. The same simulation was repeated at 40 kHz and the factor of 11.8 is within 20% of the factor at 100 kHz.

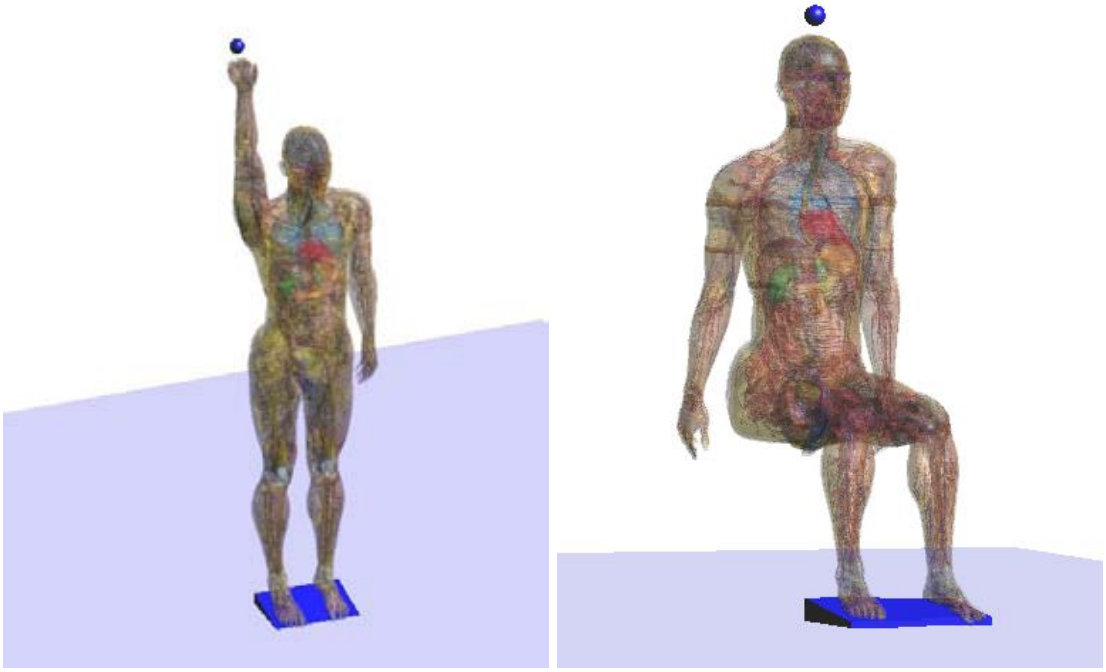

(a) Arm raised reaching for the bulb (b) Sitting posture

Figure 41: Duke model simulated in various postures with the charged sphere at three distances.

d_J (mm)	J (mA/m^2) Duke	J (mA/m^2) Probe	Ratio
Arm Raised Reaching for the Bulb			
20	300	29.3	10.2
65	140	18.2	7.7
265	47.3	8.0	5.9
20 (at 40 kHz)	139	11.7	11.8
Sitting Posture			
20	159	29.2	5.4
65	104	18.1	5.8
265	51.4	7.8	6.6

Table 19: Current densities induced in Duke model oriented in different postures and corresponding induced current densities in the current density probe from the charged sphere at three distances.

6.3.7 Interpretation of Results

The average conversion factor from Tables 16 and 17 when anatomical human models were exposed to a charged sphere located above the head was computed to be 6.1 with a standard deviation of 14.1%. Similarly, average conversion factor for uniform exposure from Table 15 for various anatomical models was computed to be 6.0 with a standard deviation of 14.5 %. Table 20 shows the scaled current densities for all ESBs (Table 10 values) after an average factor of 6.1 is taken into account to represent the current density in a person when exposed to source located above the head. Incandescent and LED bulbs are not evaluated here because their induced current density values are low compared to the noise levels of the equipment (Table 10). The highest value is approximately 56% of the ICNIRP limit. While this is still below the ICNIRP limit, it is significant. Additionally, from Table 19 it can be seen that these conversion factors could be higher by a factor of two depending on the operating frequency, posture (arm raised) and anatomical model chosen (thickness of fingers, etc., where induced currents are going to be higher due to the narrow cross-sectional area). In such a case, with worst-case conversion factors, induced current densities will be higher than those reported in Table 20.

Bulb	J_{total} (mA/m^2) rms	f_0 (kHz)	% of ICNIRP limit
E1	10.4	46.5	11.2%
E2	14.6	43.6	16.8%
E3	13.2	37.7	17.5%
E4	52.5	47.1	55.7%
E5	13.4	36.9	18.2%
E6	8.54	37.7	11.3%
E7	21.4	48.8	21.9%
E8	10.4	47.1	11.0%
E9	5.13	26.2	9.8%
E10	7.32	41.5	8.8%
E11	15.3	40.2	19.0%

Table 20: Total current density at a separation distance of 20 mm directly below the light bulb, after an average factor of 6.1 is taken into account to convert into induced levels in anatomical human models.

7 Comparison of Shielded Chamber to Different Environments

Since all the measurements (E-field, H-field and induced current density) on ESBs were conducted in a shielded environment, it is important to check the relevance of these measurements in a more realistic surroundings. Two other locations, a meeting room and an office area, were chosen to compare them with the shielded chamber. For instance, one measurement was performed under the bulb with the highest exposure (E4 bulb) hanged from the ceiling in all three locations as shown in Figure 42. Besides this, on a day-to-day basis, a person is more likely to be closer to an ESB mounted on a table lamp holder than to an ESB hanging from a ceiling. For this purpose, three lamps described in Section 3.3 were measured at closest possible distance (edge of lamp holder) with the E4 bulb in 3 locations (shielded room, meeting room and office area).

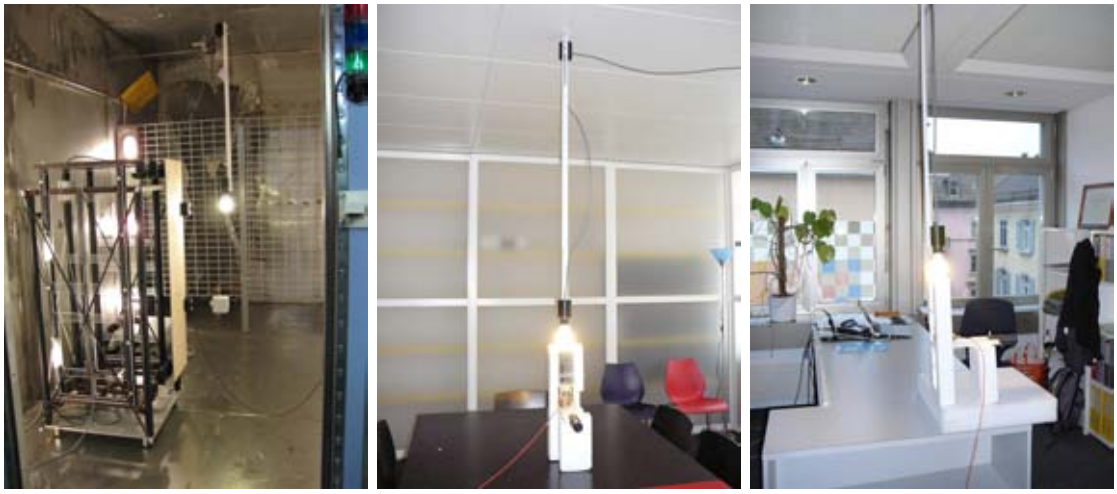

(a) Shielded Chamber (b) Meeting Room (c) Office Area

Figure 42: Bulb hanging from the ceiling is measured in different environments to test the dependance of surroundings on bulb measurements.

In the case of the reading lamp, measurements were performed below the lamp as well as to the side of the lamp (see Figure 43) since a person could be under the reading lamp. However, for the bedside lamp and standing lamp, measurements were performed only to the side of the lamp as a person is more likely to be present on the side. Worst-case human exposure from these lamps would be when a person is at closest distance to the bulb, i.e., when touching the lamp shade. Due to the presence of reinforcing foam block around the current density probe (see Figure 3), it is not physically possible to get the tip of probe to touch the lamp shade. Hence, for bedside lamp and standing lamp, three measurements were performed on the side. First, a measurement was performed with reinforcing foam block of current density probe touching the edge of lamp shade. With the current density probe fixed in this position, lamp shade (made of cloth or plastic) was removed and second measurement was performed. Finally, a third measurement was performed by moving the current density probe closer such that the tip of the probe is now at the edge of the absent lamp shade. All of these three positions on the bedside lamp and the standing lamp were shown in Figure 44. The reading lamp's metallic shade couldn't be removed/dismantled because it was an integral part of the entire lamp having the bulb holder built into it. Hence, only the first measurement was performed on the reading lamp. All electric field measurements were performed at a fixed distance of 150 mm from the center of the bulb to the center of the EHP-200 probe. In the meeting room and office area,

current density probe and EHP-200 were positioned using foam blocks (see Figure 44).

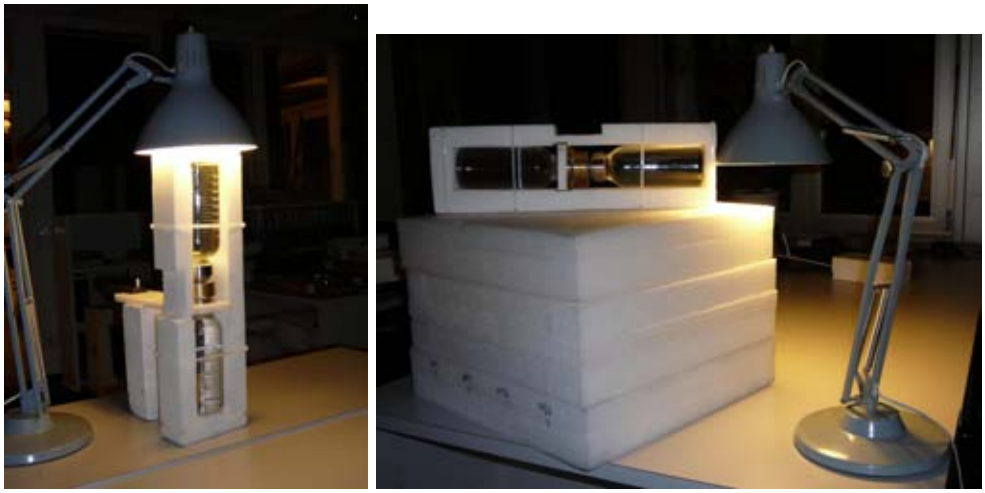

(a) Below (b) Side

Figure 43: Two measurement positions for the reading lamp.

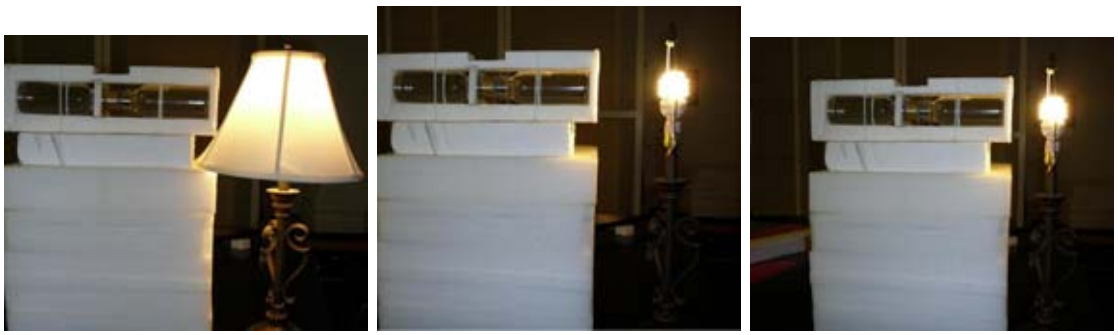

(a) With lamp shade (b) Without lamp shade (c) Without lamp shade - CLOSER

Figure 44: Three measurement positions for bedside and standing lamps.

Table 21 summarizes the electric measurements performed with Narda EHP-200 probe for all three lamps, in all three locations, and in various positions. It also provides the comparison between one environment to the other (e.g. shielded chamber vs. meeting room). Magnetic field levels were in the range of the noise level for this probe and hence was not reported for this comparison. Corresponding induced current density measurements performed with the current density probe are summarized in Table 22. From the percent difference between all three locations, it can be seen that electric-field and induced current density measurements are independant of the location. In particular for these measurements, much of this deviation between different environments arises from positioning uncertainty because of the usage of foam blocks for positioning. Moreover, this result was expected considering the fact that the fields emanating from the bulb decay rapidly with distance (see Figure 21). Thus, reflections from the surroudings are not going to significantly impact the results, especially since these measurements were performed close to the bulb. The effect of reflections from the surroundings could have been noticible had the measurements were performed far from the bulb and closer to the walls

of the surroundings. But, such a measurement wouldn't have significance since the electric-field, magnetic-field, and induced current density would be much lower than ICNIRP limits at farther distances from the bulb.

Lamp and position details	Center-center Distance (mm)	Shielded Chamber (V/m)	Meeting Room (V/m)	Office Area (V/m)	SC vs. MR	MR vs. OA	OA vs. SC
Reading Lamp - below	150	345.7	331.9	339.7	4%	-2%	-2%
Reading Lamp - side	150	60.99	53.31	60.37	14%	-12%	-1%
Bedside Lamp - without shade - side	150	348.8	339.7	367.0	3%	-7%	5%
Standing Lamp - without shade - side	150	355.2	290.2	359.3	22%	-19%	1%
Bulb hanging from ceiling - below	150	432.8	432.3	397.5	0%	9%	-8%
Average					9%	-6%	-1%
Standard Deviation					8%	9%	4%

Table 21: Electric field (E_{total} rms) around 47.5 kHz using EHP-200 probe at 150 mm distance from E4 bulb mounted inside different lamps and in Shielded Chamber (SC), Meeting Room (MR) and Office Area (OA).

Lamp and position details	Separation Distance (mm)	Shielded Chamber (mA/m^2)	Meeting Room (mA/m^2)	Office Area (mA/m^2)	SC vs. MR	MR vs. OA	OA vs. SC
Reading Lamp - below	20	5.33	5.38	5.38	-1%	0%	1%
Reading Lamp - side	95	0.72	0.86	0.88	-16%	-2%	22%
Bedside Lamp - with shade - side	144	1.05	1.06	1.11	-2%	-4%	6%
Bedside Lamp - without shade - side	144	1.64	1.52	1.58	8%	-4%	-4%
Bedside Lamp - without shade - closer - side	100	2.04	2.21	2.24	-8%	-2%	10%
Standing Lamp - with shade - side	118	1.63	2.14	2.11	-24%	2%	29%
Standing Lamp - without shade - side	118	1.68	2.26	1.90	-26%	19%	14%
Standing Lamp - without shade - closer - side	98	2.56	2.97	2.67	-14%	11%	4%
Bulb hanging from ceiling - below	20	8.67	7.34	9.84	18%	-25%	13%
Average					-7%	-1%	11%
Standard Deviation					14%	11%	10%

Table 22: Induced current density (rms) at 47.5 kHz from E4 bulb mounted inside different lamps and in Shielded Chamber (SC), Meeting Room (MR) and Office Area (OA).

8 WP5 - Validation

The measurement apparatus was validated by comparing measurements and simulations of the setup shown in Figure 45 and Figure 46. A metallic plate (435 mm x 445 mm) is placed 500 mm from the ground (metal wall). The plate was excited with a peak voltage of 10 Volts at a frequency of 100 kHz. For the measurement system, the plate was excited using an Agilent 33120A function / arbitrary waveform generator. For the simulations, the voltage of 10 Volts was defined at the metal plate. The grid resolution for the simulations of the current density probe varied from 0.4 to 10 mm.

Before placing the current density probe between the plate and ground, the electric field between the center of the metal plate and ground was simulated and measured using the Narda EHP-200 probe. The field distribution is shown in Figure 47. The measurements were within 10% of the values shown in the figure.

With the current density probe placed between the plate and ground, the electric field distribution is as shown in Figure 48. The measured current (14.67 μA) was close to the simulated current (13.65 μA), with a deviation of 7.5 %. This good agreement between measurements and simulations validates the measurement apparatus.

Figure 45: Measurement setup for validation of the current density probe.

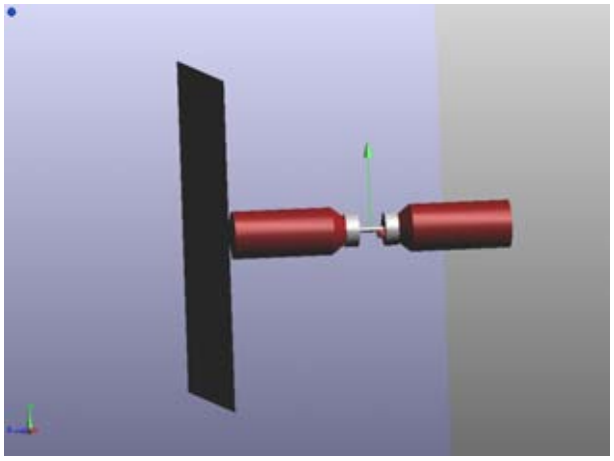

Figure 46: Simulation setup for validation of the current density probe.

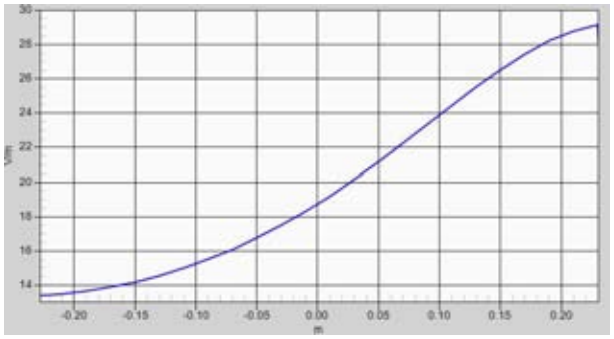

Figure 47: Electric field distribution along the centerline of the measurement setup between the two plates (i.e., along the axis of the current density probe) when the probe is not present.

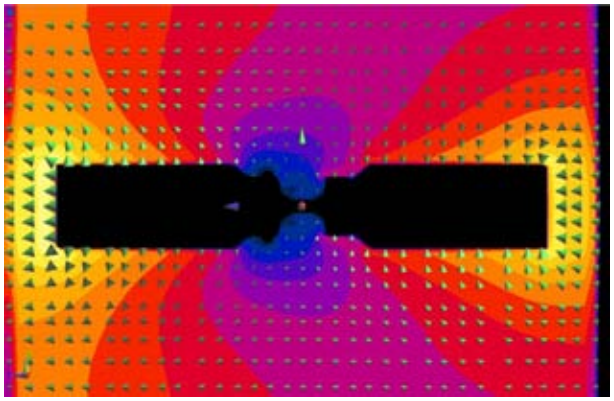

Figure 48: Electric field distribution and direction in a plane through the center of the current density probe when the probe is present.

9 WP6 - Uncertainty Evaluation

The aim of this section is to estimate the measurement uncertainty of the system used to measure the induced current density, as described in Section 4.3. The uncertainty budget and the combined uncertainty are given in the following Table.

9.1 Concept of Uncertainty Assessment

Methodologies for determining the uncertainties of experiments involving quantities that cannot be assessed by statistical means were developed for electromagnetic compatibilities, as described in, for example, Taylor and Kuyatt [28] or ISO/IEC Guide to the Expression of Uncertainty in Measurement. It has also been applied in dosimetry at radiofrequencies [29].

The methods are based on splitting the total uncertainty into various uncertainty sources that are independent or with limited interdependencies, determining the uncertainty from assumed statistical models, and calculations of the total uncertainty as the root-sum-square (RSS) value.

$$u_i = \sqrt{\sum_{i=1}^{m} c_i^2 u_i^2} \tag{24}$$

The standard uncertainty u_i evaluation will mainly based on Type B, i.e., u_i comes from the upper a_+ and lower a_- limits of the quantity in question, depending on the distribution law defining a = (a_+ - a_-)/2 , then:

- Rectangular law: $u_i = \frac{a}{\sqrt{3}}$
- Triangular law: $u_i = \frac{a}{\sqrt{6}}$
- Normal law: $u_i = \frac{a}{k}$, where k is a coverage factor
- U-shaped law: $u_i = \frac{a}{\sqrt{2}}$

In case of Type A analysis the standard uncertainty u_i is derived from the estimate from statistical observations. The offset is estimated based on the ratio of assumed worst-case conditions and evaluated conditions. The uncertainty of this ratio is treated as proportional to the offset value.

9.2 Uncertainty Budget for Measurement of Induced Current Density

The uncertainty budget for the measurement of induced current density at a distance of d_J = 50 mm has been estimated, as shown in Table 23. The expanded uncertainty is 16.7%.

9.3 Uncertainty Budget for Measurement of Incident Fields

The uncertainty budget for the measurement of incident electric field has been estimated for 300 mm distance to the light bulb, as shown in Table 24. The expanded uncertainty is nearly 40%. The sensor displacement uncertainty dominates the total uncertainty due to large size of the probe. This effect will be negligible at large distances from a source, where the field gradients are not steep. However, at 300 mm distance to the light bulbs, the field decays sharply, as seen in Figure 21. The uncertainty will likely double for measurements at the closest distance to the bulb (150 mm).

Uncertainty component	Tol. (± %)	Prob. Dist.	Divisor	Weight	Uncertainty (± %)
Source					
Bulb stability	3.5%	Rect.	1.73	1	2.0%
Probe					
Positioning w.r.t. bulb	5.0%	Rect.	1.73	1	2.9%
Positioning w.r.t. enclosure	1.9%	Rect.	1.73	1	1.1%
Orientation	4.2%	Rect.	1.73	1	2.4%
Saline dielectric properties	5.0%	Norm.	1	1	5.0%
Temperature	1.0%	Rect.	1.73	1	0.6%
Current Clamp					
Transfer impedance calculation	3.0%	Rect.	1.73	1	1.7%
Environmental Noise	1.3%	Rect.	1.73	1	0.7%
Isotropy	0.9%	Rect.	1.73	1	0.5%
Location w.r.t. probe	5.5%	Rect.	1.73	1	3.2%
Linearity	5.5%	Rect.	1.73	1	3.2%
Response time	0.0%	Rect.	1.73	1	0.0%
Frequency response	0.1%	Rect.	1.73	1	0.1%
Standard uncertainty		RSS			8.3%
Expanded uncertainty					16.7%

Table 23: Uncertainty budget for current density measurements at $d_J = 50\,\text{mm}$.

Uncertainty component	Tol. (± %)	Prob. Dist.	Divisor	Weight	Uncertainty (± %)
Bulb stability	1.2%	Rect.	1.73	1	0.7%
Positioning w.r.t. bulb	4.9%	Rect.	1.73	1	2.8%
Positioning w.r.t. enclosure	1.3%	Rect.	1.73	1	0.7%
Spherical isotropy	9.6%	Rect.	1.73	1	5.6%
Frequency response	5.9%	Rect.	1.73	1	3.4%
Sensor displacement	29.2%	Rect.	1.73	1	16.9%
Linearity	5.9%	Rect.	1.73	1	3.4%
Response time	0.0%	Rect.	1.73	1	0.0%
Averaging time	9.5%	Rect.	1.73	1	5.5%
Temperature	1.2%	Rect.	1.73	1	0.7%
Noise	2.0%	Rect.	1.73	1	1.1%
Standard Uncertainty		RSS			19.5%
Expanded Uncertainty (k = 2)					38.9%

Table 24: Uncertainty budget for electric field measurements using peak-hold detector at 300 mm from the light bulb center.

10 Mitigation Strategies

From the results in this report, the authors were able to determine that the exposure of a person to induced current density from a light bulb can vary by a factor of two or more for bulbs having the same stated output power. Aside from the rated output power, the design of the bulb therefore has a significant influence on the exposure. The light bulb consists of two parts: the electronic ballast that regulates the current to the mercury gas, and the tube which contains the mercury gas and is coated with a phosphor to emit visible light.

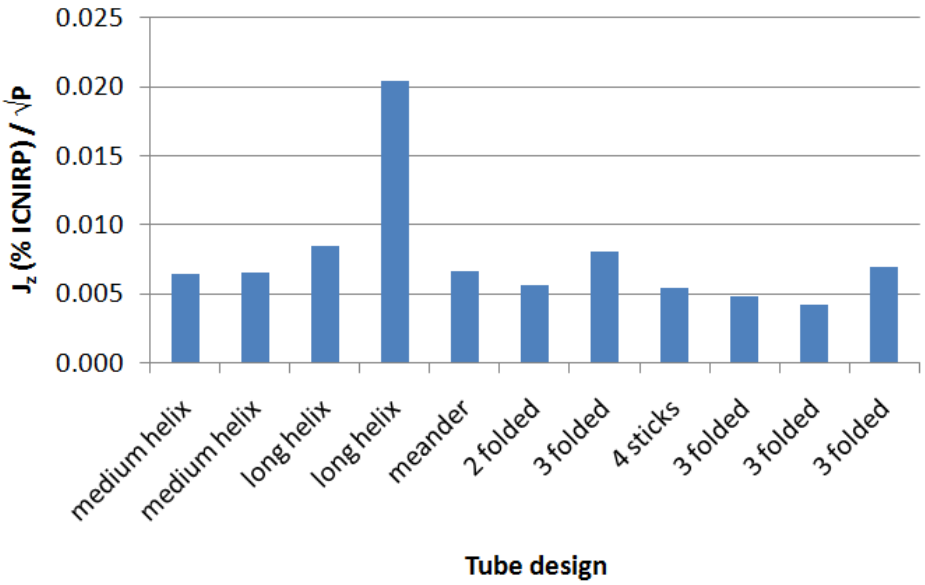

Figure 49: Normalized exposure for each of the ESBs investigated. The normalized exposure is the current density measured at a distance of $d_J = 20\,\text{mm}$ directly under the bulb, normalized to the ICNIRP limit and divided by square root of the stated output power.

To assess the influence of the tube design on the exposure, the data from Table 10 are plotted in Figure 49. The current density measured directly below the light bulb is normalized to the square root of the stated output power by the manufacturer, so that all bulbs can be compared for a fixed power level. The design of the tube is shown in the horizontal axis. It is clearly seen that for the bulbs investigated, there is no clear trend between the exposure and the tube design. This result is expected because similar looking light bulbs from different manufacturers vary significantly in terms of design. Parameters such as composition of gases in the tube, phosphor coating, efficiency of ballast (in other words, power input going into the tube from ballast circuitry) are optimized by manufacturers to obtain maximum luminous efficacy (ratio of lumens to power rating). These parameters which in turn would affect the EM parameters: discharge potential, charge distribution of ionized gases, and current flow through the tube, resulting in different field distributions and intensities for similar looking bulbs. The design of the electronic ballast also plays a significant role in the exposure. The details of the ballast design and their influence can be investigated, together with the bulb manufacturer.

The variation of the electric field at angles in the horizontal plane around the light bulb has been investigated. Figure 50 shows the result for all ESBs investigated. The incandescent and LED bulbs are not included given that the field levels are very low. The measurements were taken at a constant distance of 150 mm between the center of the probe and the center of the light bulb. The light bulb was rotated about its axis around 360 degrees. The zero degree

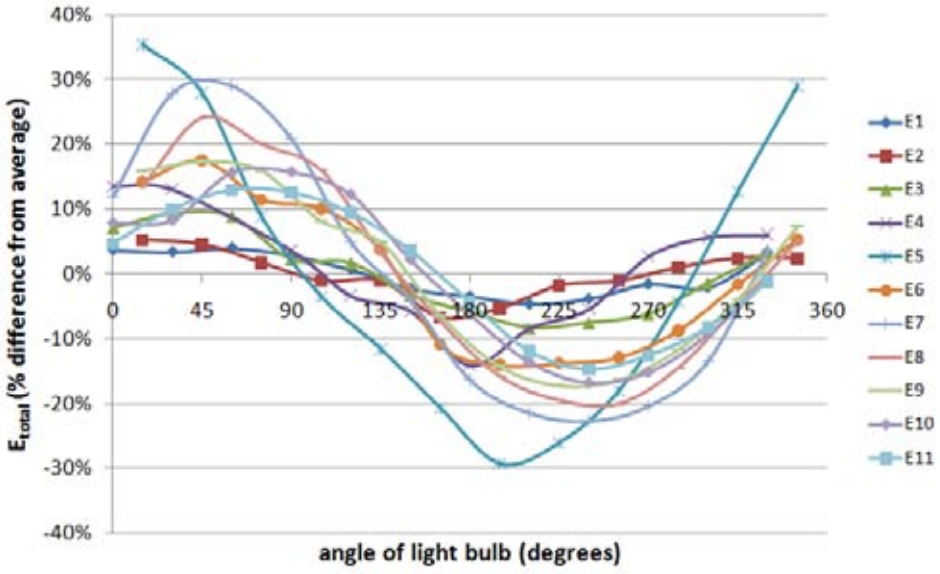

Figure 50: Total electric field measured in a horizontal plane at different angles around each of the compact fluorescent light bulbs at a center-to-center distance of 150 mm.

rotation corresponds to the location of one terminal of the fluorescent tube having the highest electric field (fluorescent bulbs have two terminals, an anode and a cathode). It is observed that for nearly all of the light bulbs, the peak field is at or near the zero degree orientation.

It was also determined in this study that the measured current densities are below the ICNIRP basic restrictions for all bulbs investigated, and that the exposure drops significantly with distance. For example, it was observed in Figure 33 that moving 200 mm away from the bulb from a close distance can reduce the exposure by a factor of five.

10.1 Grounding Lamp Shade

An additional experiment was performed on the bulb with the highest exposure (E4 bulb) mounted inside the metallic reading lamp in the two positions shown in Figure 43. Without disturbing the setup, the lamp shade was grounded and another set of measurements were performed in both those positions. As the entire lamp was made out of metal, in order to ground the lamp shade, the base of lamp was connected by a wire to the ground/earth pin of mains outlet. Table 25 shows the results of 'with' and 'without' grounding the lamp shade in both positions. Grounding the lamp shade resulted in lowering the fields emanating from the bulb. This effect was more prominant when induced currents were measured at the side of the lamp, as the grounded lamp shade partially blocks the current density probe in this position (see Figure 43(b)). In general, grounding the lamp shade would result in lowering the electric fields around the bulb since all the fields emanating from the bulb are now strongly directed towards the lamp shade. This is one possible mitigation strategy for reading and table lamps having metallic shades. Moreover, since the ground wire in the power chord is not connected to the bulb, this could be used to ground the metallic lamp shades. Additionally, in many commerical and residential locations, ESBs are mounted by recessing them into ceilings as shown in Figure 51(a). Such recessed shells usually have a metallic surface at the back to reflect the light (see Figure 51(b)). In such cases, it can be recommended to ground those reflective surfaces using the floating earth wire from the bulb's power chord to mitigate the fields emanating from the bulbs. However, such grounding is neither practical nor economical to implement.

Additionally, grounding the metal surfaces can be dangerous and is not recommended to be performed by untrained persons. One way to avoid high fields is proper selection of bulbs especially considering the fact that bulbs with similar rated output power can have significantly different exposure levels.

Lamp and position details	Separation Distance (mm)	Without grounding lamp shade (mA/m^2)	With grounding lamp shade (mA/m^2)	% change in (mA/m^2) after grounding
Reading Lamp - below	20	5.15	3.83	26%
Reading Lamp - side	95	0.63	0.31	51%

Table 25: Induced current density (rms) at 47.5 kHz in current density probe from E4 bulb mounted inside metallic reading lamp (see Figure 43) for the cases of "with" and "without" grounding this metallic lamp shade.

(a) Ceiling with recessed lighting

(b) Close-up of recessed bulb holder with metallic-reflective surface

Figure 51: An illustration of bulbs mounted inside recessed metallic shells on a ceiling.

11 Conclusions

The objective of this project is the development of scientifically sound instrumentation, methods and procedures for the EM exposure assessment of energy-saving bulbs (ESBs). Previous investigations and our initial incident field measurements have demonstrated that compliance tests cannot be performed using standard free-space equipment, since the reference levels are exceeded in the close vicinity of the light bulbs. The uncertainty of free-space measurements close to the bulbs is also very large, due to the large size of the sensors. The uncertainty is approximately ± 3 dB (± 40%) at 300 mm and will be much larger at very close distances. The recently defined standard IEC 62493 [1] is also inadequate since it is based on incident fields at an arbitrary larger distance from the bulbs (i.e., neglecting the regions of large field strength close to the bulbs) and not providing any correlation to the exposure in people.

In order to obtain a sound testing of compliance with the basic restrictions in the safety guidelines, novel equipment had to be developed for the measurement of the field values induced inside the human body. This equipment has been developed and a first prototype built, characterized and validated. The authors have also established a relationship between the measured induced current densities and the values induced in different human bodies and in various postures.

The field levels in eleven compact fluorescent ESBs, two long fluorescent tube lights, two incandescent bulbs and two LED bulbs have been measured. The results show that the primary coupling of induced current densities in the body is from the electric fields surrounding the bulbs rather than the magnetic field. For the light bulbs studied, the maximum induced current densities (at a distance of 20 mm) were comparable to the ICNIRP limits after adjusting for exposure in human body models (relative values ranged from 9% to 56% as shown in Table 20).

Over the frequency range investigated, the measured induced field levels were considerably higher for ESBs (0.84 mA/m^2 to 8.6 mA/m^2) than for LED bulbs (0.5 mA/m^2) or incandescent bulbs (within the noise level of the equipment), as shown in Table 10. The study does not represent a market overview, because not all lamps available on the market have been investigated. Thus it cannot be concluded from this study that energy saving lamps *per se* meet the ICNIRP Guidelines. Measurements of a sample of ten bulbs of the same manufacturer and model found that the variations are within the measurement uncertainty.

The measurement uncertainty of the current density probe was estimated to be 17%. The uncertainty of the conservative factors used to correlate the measured values to the induced current densities in human models is estimated to be less than 20%.

Mitigation strategies for light bulb exposure have been investigated. As expected, exposure generally increases with higher output power. However, there is considerable variation in the exposure for light bulbs having the same rated output power. The variations between different ESB models were greater than a factor of two, depending on the construction. Therefore, manufacturers can take care of the design to reduce the exposure. At locations very close to the light bulb, exposure drops strongly with distance.

In conclusion, the worst-case exposure of all investigated bulbs at a separation of 20 mm were within the ICNIRP limits, the majority of which with large margins. The maximum induced current density drops by a factor of 5 after moving 200 mm away from the bulb. However, based on the observed large variations between the bulbs, it can not be concluded that energy saving bulbs are intrinsically compliant with the ICNIRP recommendations. The exposures of the incandescent and LED bulbs were below the sensitivity of the equipment. We found that the recently defined standard procedure of IEC 62493 [1] is inadequate for determining the EM exposure of bulbs. The IEC 62493 standard can be improved by adopting the procedures and equipment described in this report.

A Standards

A.1 International Commission on Non-Ionizing Radiation Protection (ICNIRP)

Table 26: Basic restrictions for time varying electric and magnetic fields for frequencies up to 10 GHz[a] (according to ICNIRP 1998 [9]).

Exposure characteristics	Frequency range	Current density head and and trunk (mA m^{-2}) (rms)	Whole-body average SAR (W kg^{-1})	Localized SAR (head and trunk) (W kg^{-1})	Localized SAR (limbs) (W kg^{-1})
Occupational exposure	up to 1 Hz	40	—	—	—
	1 – 4 Hz	$40/f$	—	—	—
	4 Hz – 1 kHz	10	—	—	—
	1 – 100 kHz	$f/100$	—	—	—
	100 kHz – 10 MHz	$f/100$	0.4	10	20
	10 MHz – 10 GHz	—	0.4	10	20
General public exposure	up to 1 Hz	8	—	—	—
	1 – 4 Hz	$8/f$	—	—	—
	4 Hz – 1 kHz	2	—	—	—
	1 – 100 kHz	$f/500$	—	—	—
	100 kHz – 10 MHz	$f/500$	0.08	2	4
	10 MHz – 10 GHz	—	0.08	2	4

[a]Note:

1. f is the frequency in hertz.
2. Because of electrical inhomogeneity of the body, current densities should be averaged over a cross-section of 1 cm^2 perpendicular to the current direction.
3. For frequencies up to 100 kHz, peak current density values can be obtained by multiplying the rms value by $\sqrt{2}$ ($\sim$1.414). For pulses of duration t_p the equivalent frequency to apply in the basic restrictions should be calculated as $f = 1/(2t_p)$.
4. For frequencies up to 100 kHz and for pulsed magnetic fields, the maximum current density associated with the pulses can be calculated from the rise/fall times and the maximum rate of change of magnetic flux density. The induced current density can then be compared with the appropriate basic restriction.
5. All SAR values are to be averaged over any 6-min period.
6. Localized SAR averaging mass is any 10 g of contiguous tissue; the maximum SAR so obtained should be the value used for the estimation of exposure.
7. For pulses of duration t_p the equivalent frequency to apply in the basic restrictions should be calculated as $f = 1/(2t_p)$. Additionally, for pulsed exposures in the frequency range 0.3 to 10 GHz and for localized exposure of the head, in order to limit or avoid auditory effects caused by thermoelastic expansion, an additional basic restriction is recommended. This is that the SA should not exceed 10 mJ kg^{-1} for workers and 2 mJ kg^{-1} for the general public, averaged over 10 g tissue.

Table 27: Reference levels for general public exposure to time-varying electric and magnetic fields (unperturbed rms values).[a] (according to ICNIRP 1998 [9]).

Frequency range	E-field strength (V/m)	H-field strength (A/m)	B-field (μ T)	Equivalent Plane Wave Power Density S_{eq} (W/m^2)
up to 1 Hz	—	3.2 x 10^4	4 x 10^4	—
1 – 8 Hz	10,000	3.2 x $10^4/f^2$	4 x $10^4/f^2$	—
8 – 25 Hz	10,000	$4{,}000/f$	$5{,}000/f$	—
0.025 – 0.8 kHz	$250/f$	$4/f$	$5/f$	—
0.8 – 3 kHz	$250/f$	5	6.25	—
3 – 150 kHz	87	5	6.25	—
0.15 – 1 MHz	87	$0.73/f$	$0.92/f$	—
1 – 10 MHz	$87/f^{1/2}$	$0.73/f$	$0.92/f$	—
10 – 400 MHz	28	0.073	0.092	2
400 – 2,000 MHz	$1.375f^{1/2}$	$0.0037f^{1/2}$	$0.0046f^{1/2}$	$f/200$
2 – 300 GHz	61	0.16	0.2	10

[a]Note:

1. f as indicated in the frequency range column.
2. Provided that basic restrictions are met and adverse indirect effects can be excluded, field strength values can be exceeded.
3. For frequencies between 100 kHz and 10 GHz, S_{eq}, E^2, H^2, and B^2 are to averaged over any 6-min period.
4. For peak values at frequencies up to 100 kHz see Table 4, note 3.
5. For peak values at frequencies exceeding 100 kHz see Figs. 1 and 2. Between 100 kHz and 10 MHz, peak values for the field strengths are obtained by interpolation from the 1.5-fold peak at 100 kHz to the 32-fold peak at 10 MHz. For frequencies exceeding 10 MHz it is suggested that the peak equivalent plane wave power density, as averaged over the pulse width does not exceed 1,000 times the S_{eq} restrictions, or that the field strength does not exceed 32 times the field strength exposure levels given in the table.
6. For frequencies exceeding 10 GHz, S_{eq}, E^2, H^2, and B^2 are to be averaged over any $68/f^1.05$-min period (f in GHz).
7. No E-field value is provided for frequencies < 1 Hz, which are effectively static electric fields. perception of surface electric charges will not occur at field strengths less than 25 kV m$^-1$. Spark discharges causing stress or annoyance should be avoided.

Table 28: Reference levels for time varying contact currents from conductive objects[a] (ICNIRP 1998 [9]).

Exposure characteristics	Frequency range	Maximum contact current (mA)
Occupational exposure	up to 2.5 kHz	1.0
	2.5 – 100 kHz	0.4 f
	100 kHz – 110 MHz	40
General public exposure	up to 2.5 kHz	0.5
	2.5 – 100 kHz	$0.2f$
	100 kHz – 110 MHz	20

[a] f is the frequency in kHz.

Table 29: Ranges of threshold currents for indirect effects including children, women, and men.

	Threshold current (mA) at frequency:			
Indirect effect	50/60 Hz	1 kHz	100 kHz	1 MHz
Touch perception	0.2 – 0.4	0.4 – 0.8	25 – 40	25 – 40
Pain on finger contact	0.9 – 1.8	1.6 – 3.3	33 – 55	28 – 50
Painful shock/let-go threshold	8 – 16	12 – 24	112 – 224	Not determined
Severe shock/breathing difficulty	12 – 23	21 – 41	160 – 320	Not determined

Table 30: SAR limits recommended by ICNIRP [**?**].

Exposure characteristics	Frequency range	Whole-body average SAR	Localized SAR (head and trunk)	Localized SAR (limbs)
Occupational exposure	100 kHz – 10 GHz	0.4 W/kg	10 W/kg	20 W/kg
General public exposure	100 kHz – 10 GHz	0.08 W/kg	2 W/kg	4 W/kg

NOTE 1—All SAR limits are to be averaged over any six-minute interval. NOTE 2—Localized SAR averaging mass is any 10 g of contiguous tissues; the maximum SAR so obtained should be the value used for the estimation of exposure.

A.2 IEEE - ANSI - 1992

Table 31: Maximum permissible exposure for uncontrolled environments: Electromagnetic fields (according to ANSI/IEEE 1992 [13]).

Frequency range range	Electric field strength (E)	Magnetic field strength (H)	Averaging time $[E]^2$ – – $[H]^2$ [a]
3 kHz – 100 kHz	614 V/m	163 A/m	6 – – 6 minutes
100 kHz – 1.34 MHz	614 V/m	$16.3/f$ A/m	6 – – 6 minutes
1.34 MHz – 3 MHz	$823.8/f$ V/m	$16.3/f$ A/m	$f^2/0.3$ – – 6 minutes
3 MHz – 30 MHz	$823.8/f$ V/m	$16.3/f$ A/m	30 – – 6 minutes
30 MHz – 100 MHz	27.5 V/m	$158.3/f^{1.688}$ A/m	30 – – $0.0636f^{1.337}$ minutes
100 MHz – 300 MHz	27.5 V/m	0.0729 A/m	30 – – 30 minutes
300 MHz – 3 GHz			30 minutes
3 GHz – 15 GHz			$90000/f$ minutes
15 GHz – 300 GHz			$616000/f^{1.2}$ minutes

NOTE—f in MHz.

NOTE—The exposure values in terms of electric and magnetic field strengths are the values obtained by spatially averaging values over an area equivalent to the vertical cross-section of the human body.

[a]On the left is the averaging time for $|E|^2$, on the right is the averaging time for $|H|^2$. For frequencies greater than 300 MHz, the averaging time is for power density S.

Table 32: Induced and contact radiofrequency currents.

Frequency range	Maximum current (mA)		
	Through both feet	Through each foot	Contact
3 kHz – 100 kHz	$900f$	$450f$	$450f$
100 kHz – 100 MHz	90	45	45

NOTE 1—f is the frequency in MHz.

NOTE 2—It should be noted that the current limits given above may not adequately protect against startle reactions caused by transient discharges when contacting an energized object.

Table 33: SAR limits recommended by ANSI/IEEE ([13]).

Exposure characteristics	Frequency range	Whole-body average SAR	Localized SAR (partial body)	Localized SAR (hands, wrists, feet and ankles)
Controlled environment	100 kHz – 6 GHz	0.4 W/kg	8 W/kg	20 W/kg
Uncontrolled environment	100 kHz – 6 GHz	0.08 W/kg	1.6 W/kg	4 W/kg

NOTE 1—For controlled environment, the SAR limits are averaged over any six-minute interval.NOTE 2—For uncontrolled environment, the averaging time for SAR limits varies from six minutes to 30 minutes.NOTE 3—Whole-body SAR is averaged over the entire body. Partial-body SAR is averaged over any 1 g of tissue defined as a tissue volume in the shape of a cube. SAR for hands, wrists, feet and ankles is averaged over any 10 g of tissue defined as a tissue volume in the shape of a cube.

A.3 IEEE - ANSI - 2005

Table 34: Action level maximum permissible exposures (MPE for the general public when an RF safety program is unavailable) (according to IEEE Std C95.1-2005 [11]).

Frequency range	rms electric field strength (E)[a]	rms magnetic field strength (H)[a]	Averaging time[b] $[E]^2$ – – $[H]^2$ or S
100 kHz – 1.34 MHz	614 V/m	$16.3/f_M$ A/m	6 – – 6 minutes
1.34 MHz – 3 MHz	$823.8/f_M$ V/m	$16.3/f_M$ A/m	$f_M^2/0.3$ – – 6 minutes
3 MHz – 30 MHz	$823.8/f_M$ V/m	$16.3/f_M$ A/m	30 – – 6 minutes
30 MHz – 100 MHz	27.5 V/m	$158.3/f_M$ A/m	30 – – $0.0636{f_M}^{1.337}$ min.
100 MHz – 400 MHz	27.5 V/m	0.0729 A/m	30 – – 30 minutes
400 MHz – 2 GHz			30 minutes
2 GHz – 5 GHz			30 minutes
5 GHz – 30 GHz			$150/f_G$ minutes
30 GHz – 100 GHz			$25.24/f_G^{0.476}$ minutes
100 GHz – 300 GHz			$5048/[(9f_G{-}700){f_G}^{0.476}]$ m.

NOTE—f_M is the frequency in MHz, f_G is the frequency in GHz

[a]For exposures that are uniform over the dimensions of the body, such as certain far-field plane-wave exposures, the exposure field strengths and power densities are compared with the MPEs in the Table. For non-uniform exposures, the mean values of the expo- sure fields, as obtained by spatially averaging the squares the field strengths or averaging the power densities over an area equiv- alent to the vertical cross-section of the human body (projected area) or a smaller area depending on the frequency (see NOTES to the table below), are compared with the MPEs in the Table.

[b]On the left is the averaging time for $|E|^2$, on the right is the averaging time for $|H|^2$. For frequencies greater than 400 MHz, the averaging time is for power density S.

Table 35: Induced and contact rms current limits for continuous sinusoidal waveforms, f = 3 kHz to 100 kHz (IEEE Std C95.1-2005 [11]).

Condition	Action level[a] (mA)	Persons in controlled environments (mA)
Both feet	$0.90f$	$2.00f$
Each foot	$0.45f$	$1.00f$
Contact, grasp[b]	—	$1.00f$
Contact, touch	$0.167f$	$0.50f$

NOTE 1—f is the frequency in kHz

NOTE 2—Limits apply to current flowing between the body and a grounded object that may be contacted by the person.

NOTE 3—The averaging time for determination of compliance is 0.2 s.

[a]Within this frequency range the term "action level" is equivalent to the term "general public" in IEEE Std C95.6-2002 ([30]).

[b]The grasping contact limit pertains to controlled environments where personnel are trained to make grasping contact and to avoid touch contacts with conductive objects that present the possibility of painful contact.

Table 36: Induced and contact rms current limits for continuous sinusoidal waveforms, f = 100 kHz to 110 MHz (IEEE Std C95.1-2005 [11]).

Condition	Action level[a] (mA)	Persons in controlled environments (mA)
Both feet	90	200
Each foot	45	100
Contact, grasp[b]	—	100
Contact, touch	16.7	50

NOTE 1—Limits apply to current flowing between the body and a grounded object that may be contacted by the person.NOTE 2—The averaging time for determination of compliance is 6 minutes.

[a]MPE for the general public in absence of an RF safety program.[b]The grasping contact limit pertains to controlled environments where personnel are trained to make grasping
contact and to avoid touch contacts with conductive objects that present the possibility of painful contact.

Table 37: SAR limits recommended by IEEE ([11]).

Exposure characteristics	Frequency range	Whole-body average SAR	Localized SAR (head and trunk)	Localized SAR (extremities & pinnae)
Controlled environment	100 kHz – 6 GHz	0.4 W/kg	8 W/kg	20 W/kg
Action level	100 kHz – 6 GHz	0.08 W/kg	1.6 W/kg	4 W/kg

NOTE 1—For controlled environment, the SAR limits are averaged over any six-minute interval.NOTE 2—For action level, the averaging time for SAR limits varies from six minutes to 30 minutes.NOTE 3—Whole-body SAR is averaged over the entire body, partial-body SAR averaged over any 10 g of tissue defined as a tissue volume in the shape of a cube.

A.4 National Council on Radiation Protection and Measurements (NCRP)

Table 38: SAR limits recommended by NCRP ([12]).

Exposure characteristics	Frequency range	Whole-body average SAR	Localized SAR (head and trunk)	Localized SAR (limbs)
Controlled exposure	100 kHz – 10 GHz	0.4 W/kg	8 W/kg	20 W/kg
General Public exposure	100 kHz – 10 GHz	0.08 W/kg	1.6 W/kg	4 W/kg

NOTE 1—For controlled environment, the SAR limits are averaged over any six-minute interval.NOTE 2—For uncontrolled environment, the averaging time for SAR limits varies from six minutes to 30 minutes.NOTE 3—Whole-body SAR is averaged over the entire body. Partial-body SAR is averaged over any 1 g of tissue defined as a tissue volume in the shape of a cube. SAR for hands, wrists, feet and ankles is averaged over any 10 g of tissue defined as a tissue volume in the shape of a cube.

References

[1] International Electrotechnical Commission (IEC). *Assessment of lighting equipment related to human exposure to electromagnetic fields*. IEC 62493, Geneva, Switzerland, December 2009.

[2] Gregor Dürrenberger and Georg Klaus. EMF von Enegiesparlampen, Feldmessungen und Expositionsabschtzungen mit Vergleich zu anderen Quellen im Alltag. *Report of Forschungstiftung Mobilfunk (FSM)*, 2004.

[3] Georg Klaus. Response "Elektrische Felder von Energiesparlampen". 2007.

[4] Gregor Dürrenberger and Georg Klaus. Kurzkommentar zur Beurteilung von Emissionsmessungen von Energiesparlampen. 2007.

[5] Heinrich Eder. Messbericht zu Mittelfrequente electromagnetische Emmissionen durch Energiesparlampen (Stand 24.9.07). *Bayerisches Landesamt fr Umwelt, 86179 Augsburg*, 2007.

[6] Niels Kuster. Brief Review of Reported Data EM Exposure of Energy-Saving Bulbs. *Report of IT'IS Foundation*, 2008.

[7] R. Raj and G.W. King. Life prediction of tungsten filaments in incandescent lamps. *Metallurgical and Materials Transactions A*, 9(7):941–946, July 1978.

[8] U.S. Environmental Protection Agency. *Lighting Fundamentals*.

[9] ICNIRP. Guidelines for limiting exposure to time-varying electric, magnetic,and electromagnetic fields (up to 300 GHz). *Health Physics*, 74(4):494–522, 1998.

[10] Instititute of Electrical and Electronics Engineers (IEEE) SCC28. *IEEE Std C95.1 IEEE Standard for Safety Levels with Respect to Human Exposure to Radio Frequency Electromagnetic Fields, 3 kHz to 300 GHz*. IEEE Standards Department, International Committee on Electromagnetic Safety, The Institute of Electrical and Electronics Engineers, Inc. 3 Park Avenue, New York, NY 10016-5997, USA, 1999.

[11] Instititute of Electrical and Electronics Engineers (IEEE) SCC28. *IEEE Std C95.1 - 2005 IEEE Standard for Safety Levels with Respect to Human Exposure to Radio Frequency Electromagnetic Fields, 3 kHz to 300 GHz*. IEEE Standards Department, International Committee on Electromagnetic Safety, The Institute of Electrical and Electronics Engineers, Inc. 3 Park Avenue, New York, NY 10016-5997, USA, 2005.

[12] National Council on Radiation Protection and Measurements (NCRP). *Biological Effects and Exposure Criteria for Radiofrequency Electromagnetic Fields, Report 86*. NCRP, 1986.

[13] Instititute of Electrical and Electronics Engineers (IEEE) SCC28. *ANSI/IEEE. C95.1-1992, IEEE Standard for Safety Levels with Respect to Human Exposure to Radio Frequency Electromagnetic Fields, 3 kHz to 300 GHz*. IEEE Standards Department, International Committee on Electromagnetic Safety, The Institute of Electrical and Electronics Engineers, Inc. 3 Park Avenue, New York, NY 10016-5997, USA, 2005.

[14] I. Chatterjee, D. Wu, and O. Gandhi. Human body impedance and threshold currents for perception and pain for contact hazard analysis in the VLF-MF band. *IEEE Transactions on Biomedical Engineering*, 33(5):486–494, 1986.

[15] ICNIRP. Draft: Guidelines for Limiting Exposure to Time-Varying Electric and Magnetic Fields (1 khz to 100 khz), 2009.

[16] CENELEC EN50366. Household and similar electrical appliances - electromagnetic fields - methods for evaluation and measurement, May 2003.

[17] RP Blackwell. The personal current meter-A novel ankle-worn device for the measurement of RF body current in a mobile subject. *Journal of Radiological Protection*, 10(2):109–114, 1990.

[18] MJ Hagmann and TM Babij. Noninvasive measurement of current in the human body forelectromagnetic dosimetry. *Biomedical Engineering, IEEE Transactions on*, 40(5):418–423, 1993.

[19] P.K.C. Pillai, G.K. Narula, and A.K. Tripathi. Dielectric properties of polypropylene / polycarbonate polyblends. *Polymer Journal*, 16(7):575–578, 2008.

[20] C. Gabriel. Compilation of the dielectric poperties of body tissues at RF and microwwave frequencies. Technical report, Report N.AL/OE-TR-1996-0037, Occupational and environmental health directorate, Radiofrequency Radiation Division, Brooks Air Force Base, Texas (USA), June 1996.

[21] D.V. Blackham and R.D. Pollard. An improved technique for permittivity measurements using a coaxial probe. *IEEE Transactions on Instrumentation and Measurement*, 46(5):1093–1099, 1997.

[22] A. Taflove and S. C. Hagness. *Computational Electromagnetics: The Finite-Difference Time-Domain Method*. Artech House, Inc., Boston, USA, London, United Kingdom, second edition, 2000.

[23] R. Courant, K. Friedrichs, and H. Lewy. Über die partiellen Differenzengleichungen in der mathematischen Physik. *Mathematische Annalen*, 100:33–71, 1928.

[24] I. S. Kim and W. J. R. Hoefer. Numerical dispersion characteristics and stability factor for the TD-FD method. *Electronics Letters*, 26(7):485–487, March 1990.

[25] IEEE. *IEEE Std C95.3 Recommended Practice for Measurements and Computations of Radio Frequency Electromagnetic Fields With Respect to Human Exposure to Such Fields, 100 kHz–300 GHz*. IEEE Standards Department, International Committee on Electromagnetic Safety, The Institute of Electrical and Electronics Engineers, Inc. 3 Park Avenue, New York, NY 10016-5997, USA, December 2002.

[26] Andreas Christ, Wolfgang Kainz, Eckhart G. Hahn, Katharina Honegger, Marcel Zefferer, Esra Neufeld, Wolfgang Rascher, Rolf Janka, Werner Bautz, Ji Chen, Berthold Kiefer, Peter Schmitt, Hans-Peter Hollenbach, Jianxiang Shen, Michael Oberle, Dominik Szczerba, Anthony Kam, Joshua W. Guag, and Niels Kuster. The Virtual Family – development of surface-based anatomical models of two adults and two children for dosimetric simulations. *Physics in Medicine and Biology*, 55(2010):N23–N28, 2010.

[27] Emilio Cherubini, Nicolas Chavannes, and Niels Kuster. Realistic skeleton based deformation of high-resolution anatomical human models for electromagnetic simulations. In *Proceedings of the XIX General Assembly of the International Union of Radio Science (URSIGA 2008), August 7–16*, Chicago, IL, USA, August 2008.

[28] Barry N. Taylor and Chris E. Kuyatt. Guidelines for evaluating and expressing the uncertainty of NIST measurement results. Technical report, National Institute of Standards and Technology, Washington, DC, USA, 1994.

[29] IEEE. *IEEE 1528-2003, IEEE Recommended Practice for Determining the Peak Spatial-Average Specific Absorption Rate (SAR) in the Human Head from Wireless Communications Devices: Measurement Techniques*. IEEE, 445 Hoes Lane, P.O. Box 1331, Piscataway, NJ, 2005.

[30] IEEE. *IEEE Std C95.6-2002, IEEE Standard for Safety Levels with Respect to Human Exposure to Electromagnetic Fields, 03 kHz*. The Institute of Electrical and Electronics Engineers, Inc., New York, NY 10017, 2002.